HHS Public Access

Author manuscript

Cell Metab. Author manuscript; available in PMC 2024 March 07.

Published in final edited form as:

Cell Metab. 2023 March 07; 35(3): 517–534.e8. doi:10.1016/j.cmet.2023.01.010.

PHGDH-mediated endothelial metabolism drives glioblastoma resistance to chimeric antigen receptor T cell immunotherapy

Duo Zhang[1], **Albert Li**[2], **Guanghui Hu**[1], **Menggui Huang**[1], **Fan Yang**[1], **Lin Zhang**[3], **Kathryn E. Wellen**[4], **Xiaowei Xu**[5], **Crystal S Conn**[1], **Wei Zou**[1], **Mark Kahn**[6], **Seth D. Rhoades**[7], **Aalim M Weljie**[7], **Serge Y Fuchs**[8], **Nduka Amankulor**[9], **Daniel Yoshor**[9], **Jiangbin Ye**[2], **Constantinos Koumenis**[1], **Yanqing Gong**[6], **Yi Fan**[1,9,10,*]

[1]Department of Radiation Oncology, University of Pennsylvania, Philadelphia, PA 19104, USA

[2]Department of Radiation Oncology, Stanford University, Stanford, CA 94305, USA

[3]Department of Obstetrics and Gynecology, University of Pennsylvania, Philadelphia, PA 19104, USA

[4]Department of Cancer Biology, University of Pennsylvania, Philadelphia, PA 19104, USA

[5]Department of Pathology, University of Pennsylvania, Philadelphia, PA 19104, USA

[6]Department of Medicine, University of Pennsylvania, Philadelphia, PA 19104, USA

[7]Department of Systems Pharmacology and Translational Therapeutics, University of Pennsylvania, Philadelphia, PA 19104, USA

[8]Department of Biomedical Sciences, School of Veterinary Medicine, University of Pennsylvania, PA 19104, USA

[9]Department of Neurosurgery, University of Pennsylvania, Philadelphia, PA 19104, USA

[10]Lead contact

SUMMARY

The efficacy of immunotherapy is limited by the paucity of T cells delivered and infiltrated into the tumors through aberrant tumor vasculature. Here, we report that phosphoglycerate dehydrogenase (PHGDH)-mediated endothelial cell (EC) metabolism fuels formation of a hypoxic and immune-hostile vascular microenvironment, driving glioblastoma (GBM) resistance

*Correspondence to: Yi Fan, MD PhD, Department of Radiation Oncology, University of Pennsylvania, 3400 Civic Center Blvd, SCTR 8-132, Philadelphia, PA 19104, Tel: 215-898-9291; Fax: 215-898-0090; fanyi@upenn.edu.

AUTHOR CONTRIBUTIONS

D.Z. performed most of experiments, analyzed data, produced figures, and wrote the manuscript. A.L. and J.Y. contributed to metabolite tracing assays. G.H. prepared sgRNA-treated EC samples for RNAseq. M.H. and F.Y. helped EC isolation. D.Z. and L.Z. contributed to bioinformatic analysis. K.E.W., C.S.C., M.K. and Y.G. contributed to experimental design. X.X., W.Z., S.Y.F., N.A., D.Y. and C.K., contributed to discussion. S.D.R. and A.M.W. contributed to metabolome analysis. Y.F. conceived the ideas, supervised the project, and wrote the manuscript. All authors commented on the manuscript.

DECLARATION OF INTERESTS

The authors declare no competing financial interests.

to chimeric antigen receptor (CAR)-T cell immunotherapy. Our metabolome and transcriptome analyses of human and mouse GBM tumors identify that PHGDH expression and serine metabolism are preferentially altered in tumor ECs. Tumor microenvironmental cues induce ATF4-mediated PHGDH expression in ECs, triggering a redox-dependent mechanism that regulates endothelial glycolysis and leads to EC overgrowth. Genetic PHGDH ablation in ECs prunes over-sprouting vasculature, abrogates intratumoral hypoxia, and improves T cell infiltration into the tumors. PHGDH inhibition activates anti-tumor T cell immunity and sensitizes GBM to CAR T therapy. Thus, reprogramming endothelial metabolism by targeting PHGDH may offer a unique opportunity to improve T cell-based immunotherapy.

eTOC Blurb

Zhang et al report that PHGDH-mediated serine synthesis is a major altered metabolic pathway in tumor ECs. ATF4-mediated PHGDH expression stimulates glycolysis and nucleotide biosynthesis, inducing EC overgrowth. Genetic or pharmacological PHGDH inactivation prunes vasculature, improves T cell infiltration, and sensitize tumor to CAR T immunotherapy.

Graphical Abstract

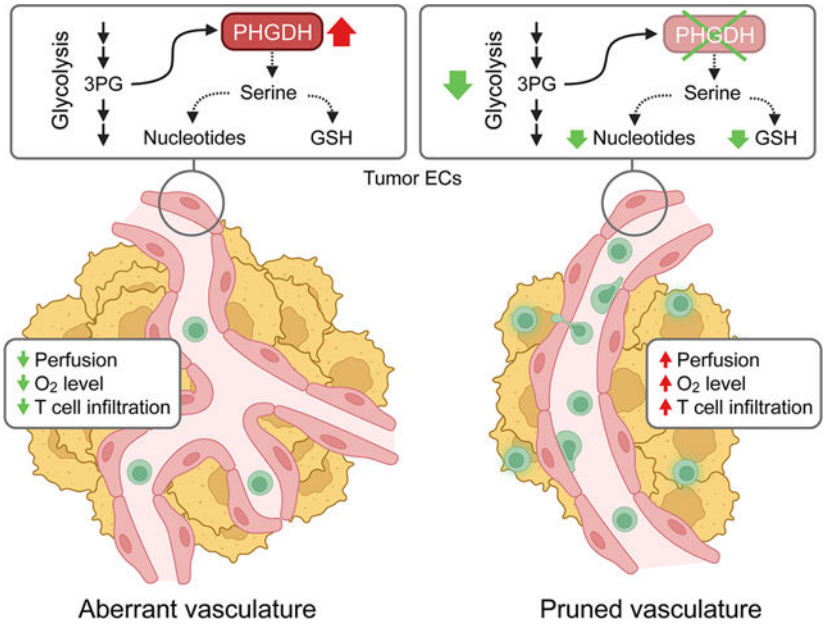

INTRODUCTION

An aberrant vascular microenvironment forms a pathophysiological barrier that hampers intratumoral T cell trafficking and renders solid tumors resistant to T cell-based immunotherapy. Tumor vasculature is characterized by manifest aberrancy in structure and function, largely due to excessive vessel outgrowth and sprouting, which impedes the delivery of T cells into the tumors [1–4]. Moreover, abnormal vasculature induces heterogenous hypoxia and forms an immune-hostile microenvironment that inhibits T cell survival and activities and induces tumor resistance to T cell-based immunotherapies,

including chimeric antigen receptor (CAR)-T therapy [5–9]. As such, targeting tumor endothelial cells to improve T cell vessel delivery and activation may serve as an emerging strategy for cancer therapy [3,4]. However, current anti-vascular therapies, that primarily target VEGF, have shown small effects on vessel normalization, eliciting transient benefits in treating most malignant cancers [10–12]. Recent studies show that perturbed endothelial metabolism induces EC dysfunction and disrupts vascular homeostasis under pathological conditions, including inflammation, diabetes, and cancer [13–22]. Particularly, endothelial metabolism may regulate tumor vascularity and immunosuppression, serving as a potential alternative target for rewiring the tumor vascular microenvironment to improve cancer immunotherapy [23].

Glioblastoma (GBM) is the most common and most aggressive malignant primary brain tumor in humans. GBM is distinguished by prominent vascularity and extraordinary vessel abnormality with a diagnostic feature of microvascular proliferation [24,25]. GBM tumors are highly resistant to cytotoxic treatments and anti-angiogenic therapies [10,12,25–28]. Moreover, GBM is also refractory to T cell-based immunotherapies, including adoptive cell transfer of chimeric antigen receptor (CAR)-modified T cells, largely due to aberrant vasculature that acts to generate an immune-hostile microenvironment, which suppresses T cell infiltration, viability, and activation [29–32]. Here, our metabolomic profiling coupled with bulk and single-cell transcriptome analyses of human and mouse tumor-derived ECs identify that stress-inducible expression of phosphoglycerate dehydrogenase (PHGDH), an enzyme that catalyzes the committed step in de novo serine biosynthesis, drives aberrant endothelial metabolism and vessel sprouting in GBM. Importantly, genetic and pharmacological ablation of PHGDH prunes over-sprouting tumor vasculature, relieves intratumoral hypoxia, activates anti-tumor T cell immunity, and improves CAR T immunotherapy in mouse GBM models. Thus, targeting PHGDH-mediated endothelial metabolism may provide a unique opportunity to improve CAR T immunotherapy in solid tumors.

RESULTS

Metabolomic and transcriptomic analyses reveal that PHGDH-mediated serine biosynthesis is a major upregulated metabolic pathway in tumor ECs

To investigate alternation in the endothelial metabolism in cancerous settings, we isolated ECs from surgical tumor specimens of human patients with GBM (Figure S1A), followed by mass spectrometry-based metabolomic analysis. $CD31^+$ ECs were sorted and validated to express vWF and to uptake Dil-Ac-LDL [33,34]. Metabolomic analysis of these tumor- and normal brain-derived ECs suggested a global metabolic alternation (Figure 1A). Further metabolite set enrichment analysis showed increased abundance of metabolites belonging to the glycine, serine, and threonine metabolism pathway in tumor ECs compared to normal ECs (Figure 1B). To define metabolic gene expression signature in these tumor ECs, we performed RNA sequencing to profile gene expression in ECs derived from tumors or treated with glioma tumor-conditioned medium, followed by mapping metabolic genes that are well characterized in 65 metabolism modules of the Kyoto encyclopedia of genes and genomes (KEGG) pathways. Interestingly, transcriptome analysis revealed that a substantial portion of metabolic genes had altered expression in tumor ECs and normal ECs under

tumor conditions (Figure 1C, left). Among the 403 metabolic genes detected, the gene sets for *i*) cysteine biosynthesis from serine and *ii*) serine biosynthesis from 3-P-glycerate were the two most affected modules (Figure 1C, right), suggesting serine synthesis as a primarily altered metabolic pathway in tumor ECs. Furthermore, specific analysis of the genes in these two modules identified that PHGDH and CBS were the most robustly upregulated 2 metabolic genes (Figure 1D). Considering that PHGDH is a rate-limiting enzyme catalyzing the committed step in *de novo* serine synthesis, we focused our study on PHGDH. In a parallel study, we characterized the expression signature of grouped 2,752 metabolic genes [35] in tumor versus normal brain ECs, showing substantial alteration of global expression in these genes (Figure S1B,C) with serine metabolism among the top upregulated pathway (Figure S1D). These findings collectively suggest that PHGDH-mediated serine synthesis is a major upregulated metabolic pathway in tumor ECs, which was verified by elevated expression of PHGDH at protein and mRNA levels in tumor ECs (Figure 1E,F).

Single-cell RNAseq analysis uncovers a critical role of PHGDH for cell cycle and proliferation regulation preferentially in tumor ECs

To explore the role of PHGDH in EC functions, we took advantage of a genetic endothelial lineage tracing system, based on tdTomato expression driven by EC-specific *Cdh5* promoter (Figure 2A), in which ECs are fluorescently labeled independent of EC-specific surface marker expression that may be altered by endothelial plasticity in cancer [33,36]. We induced GBM in a native microenvironment by implanting tumor cells isolated from a genetically engineered murine GBM model that was generated by RCAS/N-tva-mediated somatic *Pdgfb* gene transfer in *Ink4a-Arf*$^{-/-}$;*Pten*$^{-/-}$ neural stem/progenitor cells [33]. Our single-cell RNAseq analysis of tdTomato^{+} ECs (Figure 2B) showed that mouse tumor ECs had a substantially increased level of PHGDH expression, compared to normal brain-derived ECs (Figure 2C), in accordance with our bulk RNAseq results with human GBM-derived ECs. Tumor ECs exhibited a higher frequency with cells expressing the genes associated with G_2M and S cell cycle phases, suggesting tumor ECs are more proliferative (Figure 2D and Figure S2A,B). PHGDH expression was increased in proliferating ECs, particularly for tumor ECs in S phase (Figure 2E and Figure S2C). Moreover, gene set enrichment analysis showed that cell cycle and division were the most altered pathways in PHGDH^{+} versus PHGDH^{-} ECs (Figure S2D), suggesting that PHGDH expression is related to cell cycle progression and proliferation in ECs. As such, pseudotime analysis showed that the expression trajectory of PHGDH was correlated with the expression of proliferation-associated genes *Mki67*, *Top2a*, *Pcna*, and *Cenpu* in tumor ECs, but not in normal brain ECs or tumor cells (Figure 2F and Figure S2E,F), suggesting that PHGDH may be associated with cell proliferation selectively in tumor ECs. In addition, our meta-analysis of published single-cell datasets of human GBM tumors validated that PHGDH expression was upregulated during cell proliferation and correlated with Mki67 expression in tumor ECs (Figure 2G-I and Figure S2G,H). Together, these results suggest a putative role of PHGDH for cell cycle and proliferation regulation selectively in tumor ECs, but not in normal ECs or tumor cells.

PHGDH is required for cell viability and proliferation selectively in tumor ECs

To investigate the function of PHGDH in tumor ECs, we first assayed the transcriptomic effects of PHGDH knockdown. Our RT-PCR analysis verified the robust knockout efficiency by CRISPR/sgRNA (Figure 2J), and RNAseq analysis showed the resulting transcriptomic alternation (Figure 2K). Consistent with our single-cell RNAseq results suggesting a potential link of PHGDH with cell proliferation, gene set enrichment analysis of these altered genes revealed that top down-regulated pathways were associated with cell cycle progression and cell division (Figure 2L). Next, we examined the role of PHGDH in the regulation of EC proliferation.

To this end, we first tested the phenotypical effect of PHGDH loss-of-function on tumor ECs in vitro. Interestingly, treatment with WQ2101 and WQ2201, two specific and allosteric inhibitors of PHGDH [37], preferentially inhibited cell viability in tumor ECs, but not in normal ECs (Figure 2M), normal human astrocytes or glioma cells (Figure S3A). Our studies with siRNA-mediated PHGDH knockdown further confirmed that PHGDH is critical for cell proliferation in tumor ECs (Figure S3B,C). Furthermore, WQ2201 did not induce cell apoptosis (Figure S3D,E) but reduced and enhanced cell populations in S and G1/G0 phases, respectively (Figure S3E). WQ2201 markedly reduced tumor EC outgrowth and sprouting in an ex vivo tumor microenvironment system when co-cultured with human glioma cell U251 (Figure 2N). Taken together, these findings suggest PHGDH is required for cell viability and proliferation with a cell type-preferential activity toward tumor ECs.

PHGDH regulates redox homeostasis and glycolysis

Previous work suggests that PHGDH promotes malignant cell growth and tumor progression by supplying serine-dependent anabolism [38], and that PHGDH induces nucleotide and heme biosynthesis in ECs under a physiological or developmental setting [39]. To understand the function of PHGDH for metabolism and proliferation in tumor ECs, we determined the effects of PHGDH inhibition on carbon flux and redox balance that may provide and ensure metabolite demands for cell proliferation. Isotope tracing analysis showed that the WQ2201 reduced [U-^{13}C] glucose-derived carbon flux into serine and glycine, particularly at the early time points of treatment, but did not affect exogenous serine-derived flux into glycine, verifying the rate-limiting role of PHGDH for de novo serine/glycine biosynthesis (Figure 3A,B and Figure S3F). Strikingly, WQ2201 inhibited carbon flux of glycolysis and tricarboxylic acid cycle (TCA) but not pentose phosphate pathway (PPP), as indicated by decreases in the incorporation of lactate and TCA metabolites from glucose (Figure 3C-E). 2-hydroxyglutarate (2-HG), an immunosuppressive oncometabolite in glioma [40,41], can be produced by LDHA or MDH1/2 as a TCA side-product or by PHGDH from α-KG [42]. Of note, PHGDH inhibition substantially reduced the carbon flux of 2-HG from glucose (Figure 3F). In an independent study, NCT503, a different pharmacological inhibitor of PHGDH, robustly attenuated TCA metabolites and 2-HG (Figure S3G-I), validating the critical role of PHGDH for regulating glycolysis and the TCA cycle. Moreover, WQ2201 disrupted glucose-derived nucleotide biosynthesis, as indicated by inhibited ADP, ATP, UDP, and UTP incorporation from glucose (Figure 3G) and reduced cellular ATP and UTP levels (Figure S3J-L), and reduced carbon flux of TCA (Figure S3M), in agreement with a recent report showing PHGDH regulates central carbon and nucleotide metabolism in tumor cells [43]. In

addition, a siRNA-mediated knockdown study confirmed these metabolic phenotypes, as indicated by that PHGDH knockdown reduced carbon flux of glycolysis and TCA in tumor ECs (Figure S4).

Serine biosynthesis and one-carbon metabolism are coupled with cysteine biosynthesis, in which the key enzyme cystathionine-β-synthase (CBS) was also upregulated in tumor ECs (Figure 1D), likely driving the production of glutathione (GSH), a key reducing metabolite in maintaining redox homeostasis. Consistent with the requisite role of PHGDH for serine biosynthesis, our data showed that WQ2201 markedly reduced total cellular glutathione (GSH+GSSG; GSSG, the oxidized form of GSH) levels and the ratio of GSH/GSSG (Figure 3H,I). Furthermore, in accordance with the fact that PHGDH consumes 3-phosphoglycerate and NAD+ to generate 3-phosphohydroxypyruvate and NADH, our data showed that WQ2201 attenuated cellular NADH level and enhanced NAD^+/NADH ratio (Figure 3J,K), collectively indicating that PHGDH regulates redox homeostasis in tumor ECs. Thus, these findings suggest that PHGDH regulates nucleotide synthesis, central carbon flux, and redox homeostasis, which contributes to tumor EC proliferation. To test this hypothesis and to determine which metabolic processes may be involved in the effects of PHGDH inhibition on cell proliferation, we supplemented serine/glycine-deprived tumor ECs with various metabolites related to PHGDH metabolism in the presence of WQ2201, including cell-permeable α-ketoglutarate, 2-hydroxyglutarate, nucleosides, formate, hemin, and antioxidants. Our data showed that only the addition of nucleosides and antioxidants, including dithiothreitol, N-acetylcysteine, and GSH, partially rescued cell proliferation from PHGDH inhibition (Figure 3L), indicating two major functions of PHGDH for cell proliferation are to promote nucleotide synthesis and to keep redox balance in tumor ECs. Interestingly, GSH supplementation rescued glucose incorporation into glycolysis, rather than the TCA cycle, from PHGDH inhibition, as indicated by restored 3-phosphoglycerate (3-PG), phosphoenolpyruvate (PEP), and pyruvate carbon flux (Figure 3M and Figure S3M), suggesting that PHGDH regulates redox to selectively modulate glycolysis, consistent with a previous report showing that glycolysis is a preferential metabolic pathway in ECs [13]. Together, these findings suggest that PHGDH promotes nucleotide biosynthesis and maintains redox homeostasis to support preferential glycolysis, contributing to cell proliferation in tumor ECs.

Tumor microenvironmental cues activate ATF4, inducing PHGDH expression

We next explored the mechanism by which PHGDH expression is upregulated in tumor ECs, initially focusing on its transcriptional regulation. We identified 90 transcriptional factors (TFs) that potentially bind to PHGDH promoter based on bioinformatics prediction, and among them, 18 – 36 TFs were upregulated in tumor ECs or normal ECs treated with glioma-conditioned medium with 12 TFs upregulated in both conditions (Figure 4A). Pathway set analysis of these upregulated TFs revealed that the top regulated pathway was related to ATF4 (Figure 4B), which is a master TF that controls cellular responses to stress and plays an important role in tumor microenvironment [44]. Our data showed that siRNA-mediated knockdown of ATF4 and its regulator and binding partner NRF2 [45,46] abrogated PHGDH expression at protein and mRNA levels (Figure 4C,D). Likewise, pharmacological inhibition of ATF4 by ISRIB reduced PHGDH expression, while activation

of ATF4 by thapsigargin stimulated PHGDH expression (Figure 4E), suggesting a requisite role of ATF4 for PHGDH expression in ECs. Furthermore, our ChIP analysis showed a robust activity of ATF4 binding to PHGDH promoter, particularly at the region of +912 to +988 bp downstream of TSS, in tumor ECs, and to a lesser extent (with ~20% binding activity), in normal ECs (Figure 4F), providing a mechanism for ATF4 hyperactivation-driven PHGDH expression in tumor ECs. In addition, ATF4 activation in ECs was also inducible under tumor conditions with excessive secretory factors including VEGF-A, as indicated by that VEGF-A and tumor-conditioned medium increased PHGDH expression in an ATF4-dependent manner (Figure 4G). Similarly, hypoxia and serine/glycine deprivation, two common features in the GBM tumor microenvironment, stimulated ATF4-dependent PHGDH expression (Figure 4H), collectively suggesting that tumor microenvironmental stress induces PHGDH expression via ATF4. As such, VEGF-A, tumor-conditioned medium, hypoxia, and deprivation of serine/glycine substantially promoted ATF4 binding to PHGDH promoter and cis-regulatory element (Figure 4I,J). Finally, ATF4 knockdown inhibited cell proliferation in tumor ECs but not normal ECs (Figure 4K), in which cell growth was monitored over time and measured based on calcein AM staining. These results suggest that tumor microenvironmental cues activate ATF4, leading to ATF4-mediated PHGDH transcriptional activation and overexpression in ECs.

Genetic PHGDH ablation reduces vascular aberrancy, improves T cell infiltration, and inhibits GBM growth

We then sought to examine the in vivo roles of PHGDH for tumor vascularization and progression. We generated EC-specific Phgdh knockout and knockdown lineage-tracing mouse lines, called *Cdh5-Cre*^{ERT2};*Phgdh*$^{fl/fl}$ and *Cdh5-Cre*^{ERT2};*Phgdh*$^{fl/+}$, respectively, by crossing a newly generated *Phgdh*$^{fl/fl}$ mice, i.e., by flanking exon 2 of *Phgdh* by two LoxP sites, with mice expressing Cre under the EC-specific promoter *Cdh5* (Figure 5A). Consistent with a recent report showing *Pdgfb-Cre*-driven deletion of PHGDH in ECs induced lethality in mice [39], our data showed that tamoxifen-inducible homozygous PHGDH knockout caused lethality within 3 weeks after tamoxifen injection in neonatal mice (Figure S5A,B), which led us to focus our study using mice with heterogyzygous knockout, i.e., Phgdh knockdown. RT-PCR verified Phgdh knockdown efficiency of about 50% in tdTomato^{+} mouse brain and aorta ECs (Figure 5A). We then challenged these mice with an orthotopic injection of the tumor cells isolated from the RCAS-mediated genetically engineered GBM model (Figure 5B). Our results showed that the EC-specific Phgdh knockdown improved animal survival (Figure 5C). Likewise, Phgdh knockdown inhibited tumor growth (Figure 5D). In addition, the bioluminescence signal drops in few mice suggest that their critical condition was approaching to the end point, possibly due to dysfunctional circulation and perfusion in these dying mice.

To examine the effects of genetic Phgdh ablation on tumor vascularization, GBM was induced in control and PHGDH-EC^{Knockdown} (KD) mice with tdTomato expression in ECs (Figure 5E). We took advantage of light sheet fluorescence imaging technology that allows us to visualize tumor vasculature at a whole-organ level. Our data showed that Phgdh knockdown induced a “vessel pruning” effect, apparently altering the chaotic morphology (tortuous vessels with excessive sprouts) and resulting in a well-organized structure (defined

vessels with fewer sprouts) in tumor-associated vasculature, as indicated by reduced vessel volume, area, and length (Figure 5F). Moreover, Phgdh knockdown led to a marked reduction, by > 90%, in intratumoral hypoxia (Figure 5F), suggesting that the tumor microenvironment is reconditioned as perfusion improved. Interestingly, Phgdh knockdown robustly stimulated T cell infiltration into the tumors (Figure 5G), likely contributing to the inhibition of tumor growth. Consistent with these findings, antibody-mediated depletion of $CD3^+$ T cells abolished the effects of improved survival and inhibited tumor growth in PHGDH-EC^{KD} mice (Figure S5C,D), suggesting a T cell-dependent survival mechanism. Together, these results suggest that endothelial PHGDH is critical for vascular aberrancy, intratumoral hypoxia, inhibition of T cell infiltration, and tumor growth.

PHGDH inhibition prunes tumor vasculature and improves T cell infiltration and activation

We next investigated the effects of WQ2201, a pharmacological PHGDH inhibitor showing robust bioactivity, tolerability, and selectivity for PHGDH in vivo [37], on vascular morphology and T cell infiltration and function in GBM (Figure 6A). Treatment with WQ2201 elicited robust vessel pruning phenotypes similar to that induced by PHGDH knockdown, including reduction of tumor vessel aberrancy, volume, area, and length and intratumoral hypoxia (Figure 6B and Figure S6A). As such, WQ2201 treatment markedly improved T cell infiltration into the tumors (Figure 6C and Figure S6B). In addition, WQ2201 did not affect vasculature in normal brains (Figure S6C,D). Given the critical role of PHGDH for induction of intratumor hypoxia and production of 2-HG that can modulate T cell activity [41,47,48], we examined the effects of PHGDH inhibition on T cell functions in the tumors. Our CyTOF analysis showed that WQ2201 treatment induced broad changes to immune cell infiltration (Figure 6D and Figure S6E), and enhanced the infiltration of $CD3^+$ T cells into the tumor, specifically enhancing the population of $CD8^+$ cytotoxic T cells but not significantly affecting $CD4^+Foxp3^+$ regulatory T cells (Figure 6E). Of particular significance, WQ2201 treatment robustly improved T cell activation, as indicated by increases in expression of T cell effector molecules including IFN-γ and granzyme B and proliferative marker Ki67 (Figure 6F). Similarly, our flow cytometry analysis confirmed these beneficial effects on anti-tumor T cell immunity, showing that WQ2201 treatment stimulated T cell infiltration (Figure 6G), reduced macrophage recruitment (Figure S6F), increased the CD8 population and decreased the ratio of CD4/CD8 T cells (Figure 6H). These results collectively suggest that PHGDH inhibition promotes T cell infiltration into and activation at the tumors.

PHGDH inhibition improves CAR T immunotherapy in two preclinical mouse GBM models

Based on our observation that PHGDH knockdown in ECs led to pruned tumor vasculature and enhanced T cell infiltration into the tumors (Figure 5), and that PHGDH inhibition reconditioned tumor immune microenvironment and activated T cells (Figure 6), we investigated the effects of PHGDH inhibition on cell trafficking and therapeutic efficacy of CAR T cells using a murine 139 scFV CAR T system that was recently developed to target Egfrviii, a GBM-associated EGFR mutant [49,50]. To visualize CAR T cells, mice bearing RCAS-induced genetically engineered $fLuc^+$ GBM tumors (40% heterogenous $Egfrviii^+$ tumor cells by lentiviral transduction) were intravenously infused with Egfrviii CAR T cells expressing nanoLuc (nLuc), following WQ2201 treatment, and imaged by whole-body

bioluminescence (Figure 7A). Our data showed a selective homing of nLuc$^+$ CAR T cells into the tumors, and that WQ2201 treatment markedly improved the T cell infiltration, leading to a longer persistence over time (Figure 7B). Inspired by these results, we next investigated the effects of PHGDH inhibition on CAR T immunotherapy using two mouse GBM models including syngeneic GL261 (100% Egfrviii$^+$ tumor cells) and heterogenous Egfrviii$^+$ RCAS GBM tumors (Figure 7A). Our data showed that WQ2201 monotherapy did not significantly affect mouse survival ($P > 0.05$, Figure 7C,D) or tumor growth (Figure 7E,F) in both tumor models. Furthermore, CAR T immunotherapy alone only slightly improved mouse survival, as indicated by +7.5 days from the control group with median survival of 25 days in RCAS tumors as well as +3 days from the control group with median survival of 16 days in GL261 tumors. As such, CAR T immunotherapy alone also failed to robustly inhibit tumor growth. In contrast, WQ2201 treatment sensitized tumors to CAR T immunotherapy, as indicated by substantial increases in mouse survival including +17 days in RACS tumors and +12.5 days in GL261 tumors. The combination therapy robustly delayed tumor growth in both tumor models. Notably, nearly 60% and 30% of the mice in the combination therapy group still survived even when all of the mice in the other groups had died by 37 and 34 days after tumor induction in RCAS and GL261 tumors, respectively. Importantly, the combination therapy induced complete tumor regression in 10%−20% of mice. These results indicate that PHGDH inhibition sensitizes GBM tumors to CAR T immunotherapy.

In addition, we tested the effects of pharmacological inhibitions of VEGF pathway on tumor sensitivity to CAR T cell therapy. Mice bearing Egfrviii$^+$ GL261 glioma tumors were administered with a DC101 anti-mouse VEGFR2 antibody that blocks VEGF/VEGFR2 signaling, followed by treatment with CAR T cells. Our data showed that VEGFR2 blockade did not improve animal survival or inhibit tumor growth, as indicated by +1 day from the control group with median survival of 25 days with $P > 0.1$ (Figure S7). Moreover, VEGFR2 blockade also did not sensitize tumors to Egfrviii CAR T cell therapy, as indicated by +1.5 day from the control IgG-treated Egfrviii CAR T group with median survival of 19.5 days with $P > 0.5$.

Taken together, the results of our experiments identify PHGDH-mediated serine metabolism as a major altered metabolic pathway in GBM ECs (Figure 7G). We uncovered a PHGDH-mediated mechanism that regulates redox homeostasis and central carbon metabolism in tumor ECs, driving excessive EC proliferation and vessel sprouting, which leads to formation of a hypoxic and immune-hostile microenvironment that inhibits T cell infiltration into and activation at the tumors. We show that PHGDH inhibition prunes tumor vasculature, recondition tumor microenvironment and improves CAR T immunotherapy in vivo.

DISCUSSION

A major challenge that exists for implementing immunotherapy of solid tumors by adoptive lymphocyte transfer is the abnormal tumor vasculature that impedes lymphocyte delivery and infiltration into the tumors and generates a hypoxic tumor microenvironment that undermines viability and activities of those lymphocytes. As such, immunotherapy with CAR-engineered T cells shows promise for treating solid tumors, including GBM [51–53];

however, it has encountered major therapeutic difficulties in clinic, largely due to limited T cell infiltration into and activation at the tumors, particularly for those immunologically inert tumors such as GBM [30]. Thus, targeting aberrant tumor vasculature represents an emerging strategy for improving immunotherapy. In the present study, our metabolomic and transcriptome analyses of human and mouse tumor ECs identify PHGDH as a pathologically-specific regulator of endothelial metabolism and vessel abnormalities in GBM. Genetic and pharmacological ablation of PHGDH prunes over-sprouting tumor vasculature, enhances T cell recruitment to and activation in the tumor, and sensitizes GBM to CAR T immunotherapy, likely due to *i)* improved vessel delivery of T cells, *ii)* relieved tumor hypoxia, and *iii)* reduced production of immunosuppressive EC metabolites in the vascular niche, all facilitating T cell infiltration and activation (Figure 7G). Monotherapy with PHGDH inhibition could not induce robust therapeutic efficacy due to a paucity of brain tumor infiltrates with endogenous T cells, but its combination with infusion of massive CAR T cells may induce sufficient T cell infiltration to drive anti-tumor effects. These findings suggest that metabolically reprogramming tumor ECs, which joins genetic EC reprogramming [50,54], may serve as a promising strategy for rewiring tumor vascular microenvironment to improve cancer immunotherapy [23]. In addition, we suggest that structurally normalizing vasculature and relieving tumor hypoxia by PHGDH inhibition may also improve drug delivery and sensitize tumor to cytotoxic treatment, leading to improved tumor responses to molecular targeted therapy and radio/chemotherapy.

Endothelial metabolism has recently been recognized as a driving force or key regulator of EC function, vascular homeostasis, and sprouting angiogenesis, with distinct metabolic pathways including glycolysis, fatty acid oxidation, and glutamine metabolism identified in ECs [13–22]. Consistent with a preferential and requisite role of glycolysis for EC metabolism and function, genetic loss or pharmacological blockade of 6-phosphofructo-2-kinase/fructose-2,6-bisphosphatase 3 (PFKFB3), a key regulator of glycolysis, inhibits EC proliferation and migration and reduces vessel sprouting in physiological and pathological conditions of inflammation and tissue injury, as well as normalizes tumor vessels and impairs metastasis [13,55,56]. Strikingly, our results show that PHGDH inhibition reduces glycolysis, as evidenced by reduced flux of glucose-derived carbons to pyruvate (−60%, Figure 3M) and to lactate in tumor ECs (−30–50%, Figure 3C,M), suggesting that PHGDH regulates EC proliferation and vessel sprouting, at least in part, through modulating glycolysis. An elegant recent study shows that PHGDH reduces oxidative stress by synthesizing heme to maintain mitochondrial respiration and homeostasis, in addition to inducing GSH and NADPH synthesis, in normal ECs [39]. In accordance with these findings, our study shows that PHGDH is critical for GSH biosynthesis and NADH production that maintain redox balance in tumor ECs. Interestingly, supplementation with GSH, but not hemin, rescues cell proliferation in PHGDH-inhibited tumor ECs (Figure 3H), suggesting a pathologically specific effect in tumor conditions. Our work reveals a central role for PHGDH in endothelial metabolism-mediated vessel abnormality and tumor hypoxia, which inhibits T cell infiltration into the tumor. In addition, PHGDH also induces EC production of lactate and 2-HG, two metabolites that inhibit cytotoxicity functions in T cells [41,48,57], contributing to formation of an immunosuppressive vascular niche and tumor resistance to CAR T immunotherapy.

As a frequently upregulated metabolic pathway in cancer cells, serine metabolism generates carbon units required to *de novo* synthesis of nucleotide precursors for anabolic metabolism and of GSH for redox homeostasis maintenance, promoting cancer cell proliferation and tumor growth [35,38,58–63]. Likewise, our work reveals that PHGDH expression is upregulated in tumor ECs via tumor microenvironmental stress- and VEGF-induced ATF4 activation, driving EC proliferation and vessel sprouting. Consistently, PHGDH exhibits copy-number gain and ATF4/NRF2-mediated transcription in cancer cells [35,46,64]. Given generation of NADH to support oxidation reaction and biomass synthesis is a metabolic constraint for PHGDH-mediated serine biosynthesis and cell proliferation [65,66], our data show that PHGDH regulates cellular NAD^+/NADH ratio and induces a balanced redox state that contributes to carbon flux in glycolysis, suggesting a potential forward feedback loop that drives NAD(H) production, central carbon flux, and serine metabolism in tumor ECs. Supportive of our findings, a recent study shows that PHGDH inhibition disrupts the mass balance within central carbon metabolism such as glycolysis and TCA cycle in tumor cells [43]. Regulation of central carbon metabolism by PHGDH could be due to transamination reaction downstream of PHGDH that converts glutamate to αKG to fuel the TCA cycle in tumor cells [43,67]; however, our results show that supplementation with αKG fails to rescue PHGDH inhibition-induced phenotypes, suggesting an elusive mechanism by which PHGDH regulates the TCA cycle in tumor ECs. Our work establishes an integrated role for PHGDH in GSH synthesis and NADH production to maintain redox balance that is required to drive preferential glycolysis for energy and biomass production in ECs, in addition to its role in nucleotide synthesis following serine/glycine metabolism, both facilitating vessel outgrowth and sprouting in cancer.

In summary, our work uncovers a requisite role of PHGDH in perturbed endothelial metabolism, aberrant vascularization, and suppressive T cell immunity in GBM. We suggest that the therapeutic efficacy associated with enhanced T cell delivery and activation by PHGDH inhibition can be further improved when combined with other immunotherapy approaches capable of increasing T cell persistence by inhibiting T cell exhaustion and/or by stimulating their T cell activation in the tumor microenvironment. Thus, targeting PHGDH-mediated endothelial metabolism may provide a unique opportunity to recondition tumor vascular-immune microenvironment and improve immunotherapy for treating solid tumors.

Limitations of Study

Most of our in vivo studies were based on murine GBM models that do not capture the diverse heterogeneity of human glioma. Future work using immune-humanized patient-derived xenograft (PDX) models will be needed to validate our results, which will provide further information for potential clinical treatment in humans. In the present work, we have tested experimental therapy that combines PHGDH inhibition with CAR T immunotherapy, and the effects of PHGDH inhibition on tumor resistance to other T cell immunotherapies including immune checkpoint blockade remain unknown. In addition, our study has a focus on GBM; however, considering aberrant vascularity is a common feature of most malignant solid tumors, pharmacological inhibition of PHGDH may also improve tumor response to T cell-based immunotherapy in other cancer types, which needs further investigation.

STAR METHODS

RESOURCES AVAILABILITY

Lead contact—Further information and requests for resources and reagents should be directed to and will be fulfilled by the lead contact, Yi Fan (fanyi@upenn.edu).

Materials availability—All unique reagents including mouse lines that were generated in the course of this study are available from the lead contact with a completed Materials Transfer Agreement.

Data and code availability

- All the bulk and single-cell RNA-seq data have been deposited at NCBI's Gene Expression Omnibus (GEO) and are publicly available as of the date of publication. Accession numbers are listed in the key resources table. Uncropped blots and values of graphs are included in the zip file, Data S1.
- No original code was generated in this study.
- Any additional information required to reanalyze the data reported in this paper is available from the lead contact upon request.

EXPERIMENTAL MODEL AND SUBJECT DETAILS

Mice—*Phgdh*$^{fl/fl}$ mice on C57BL/6 background were generated by inserting two LoxP sequences into the flanks of exon 2 of *Phgdh* gene and genetically validated by the University of Pennsylvania Transgenic and Chimeric Mouse Facility. *Cdh5-Cre*^{ERT2};*Rosa-LSL-tdTomato* mice on C57BL/6 background were generated by crossing *Rosa-LSL-tdTomato* mice (Jackson Laboratory, 007914) with *Cdh5-Cre*^{ERT2} mice (provided by Ralf Adams at Max Planck Institute). *Cdh5-Cre*^{ERT2};*Rosa-LSL-tdTomato*;*Phgdh*$^{fl/wt}$ mice were generated by crossing *Cdh5-Cre*^{ERT2};*Rosa-LSL-tdTomato* mice and. Mice (2 weeks old, half male and half female) were intraperitoneally injected with 80 mg/kg tamoxifen daily for consecutive 5 days. Genetically engineered GBMs were induced in mice as described previously[33]. In brief, chicken DF-1 fibroblasts (American Type Culture Collection, CRL-12203) were transfected with *RCAS-PDGF-B* and *RCAS-Cre* plasmids to produce retrovirus, followed by orthotopic injection into *Ntv-a*;*Ink4a-Arf*$^{-/-}$;*Pten*$^{fl/fl}$;*LSL-luc* mice (8 weeks old, half male and half female) to induce GBM. Tumors were isolated and subjected to mechanical dissociation with a gentleMACS Dissociator (Miltenyi Biotec) and enzymatic digestion using collagenase II (Invitrogen, 17101–015) and dispase II (Gibco, 17105–041) to obtain single-cell suspensions. Tumor-derived single-cell suspensions were cultured with NeuroCult mouse stem cell medium (Stemcell Technologies, 5702). For RCAS-mouse Egfrviii model, isolated RCAS tumor cells were lentivirally transduced to co-express mouse Egfrviii and green fluorescent by incubating the tumor-derived sphere cells with the filtered lentivirus-containing supernatant for 24 h in mouse stem cell medium with 4 μg/ml protamin sulfate (MP biomedicals, 02194729-CF). Attached cells were discarded to remove tumor stromal cells, and non-adherent sphere-forming tumor cells were injected into mouse brains. For the syngeneic GBM model, mouse GL261 glioma cells were lentivirally transduced to co-express mouse Egfrviii and green fluorescent protein, and green fluorescent protein-

positive cells were harvested by cell sorting. Approximately 8-week-old C57BL/6 mice (half male and half female) were orthotopically and stereotactically injected with 10^5 of either type of GBM tumor cells in a total volume of 1 μl. For T cell depletion, mice were injected intravenously with 2 mg/kg anti-mouse CD3ε F(ab')2 fragment (BioXCell, BE0001–1FAB) or hamster IgG f(ab')2 fragments (BioXCell, BE0091-FAB) for consecutive 5 day, starting 7 days after injection of tumor cells. For VEGFR2 blockade study, mice were administrated intravenously with 25 mg/kg anti-mouse VEGFR-2 (DC101, BioXCell, BE0060) or control rat IgG1 isotype (BioXCell, BE0088) for three doses, respectively 6, 8, and 10 days after injection with tumor cells. Tumor growth was monitored by bioluminescence using an IVIS 200 Spectrum Imaging System (Perkin Elmer) after retro-orbital injection of D-luciferin (150 mg/kg; GoldBio, LUCNA-5G). For T cell imaging, mice that were injected with nLuc-expressing mouse T cells were imaged after retro-orbital injection of furimazine (0.5 mg/kg in 10% DMSO, TargetMol, T15359) at least 40 min before the D-luciferin injection for imaging the tumor cells. Mice were peritoneally administrated with saline or 10 mg/kg WQ-2201 (Biotechne, 6581). Mouse CAR-T cells were introduced retro-orbitally after GBM induction. Post-injection survival was monitored for up to 60 days. Mice were euthanized when exhibiting severe GBM symptoms including domehead, hemiparesis or more than 20% of body weight loss. All animals were housed at room temperature with a 12-h light/12-h dark cycle at an Association for Assessment and Accreditation of Laboratory Animal Care-accredited animal facility of the University of Pennsylvania. All experiments with mice were performed in accordance with an animal protocol approved by the Institutional Animal Care and Use Committee at the University of Pennsylvania.

Human ECs—Surgical specimens from human patients with GBM were collected at the Department of Neurosurgery of the Hospital of the University of Pennsylvania. The collection of human tissues in compliance with the tissue banking protocol was approved by the University of Pennsylvania Institutional Review Board, and written informed consent was obtained from each participant. ECs were isolated and verified as previously described [33,34]. In brief, tumor-derived single-cell suspensions were prepared by the tissue bank. Cell suspensions were subjected to magnetic activating cell sorting (MACS) with anti-CD31 antibody-conjugated magnetic beads (Miltenyi Biotech, 130–091-935). Sorted ECs were verified by Dil-Ac-LDL (Alfa Aesar, J65597) absorption and vWF staining. Human brain microvascular ECs (isolated from human brains; ScienCell, 1000; Cell Biologics, H6023) were maintained in Endothelial Cell Growth Medium 2 (PromoCell, C-22211 and C-39211) unless specified otherwise. Cells were checked and showed no mycoplasma contamination. All cells were used between passages 2 and 6. ECs were incubated in Ser/Gly-depleted medium (glucose-, serine-, and glycine-free Endothelial Cell Growth Medium 2, PromoCell, custom order) supplemented with 5% dialyzed FBS (Gibco, A3382001) and 5.5 mM glucose (Sigma Aldrich, G8270) under normoxic or hypoxic condition (1% O_2), or treated with VEGF (50 ng/ml, PeproTech, 100–20). For the viability assays, ECs were cultured in the Ser/Gly-depletion medium and treated with 150 μM WQ-2201 (Biotechne, 6581) in combination with serine (300 μM, Sigma Aldrich, S4311) and glycine (30 μM, Sigma Aldrich, G8790), dimethyl-α-KG (1 mM, Sigma Aldrich, 349631), 2-hydroxyglutarate (500 μM, Sigma Aldrich, 94577), nucleosides (50 x, Sigma Aldrich, ES-008-D), dNTPs (300 μM, Thermo Scientific, 10297018), formate (1 mM, Sigma Aldrich, 71539), hemin

(30 μM, Sigma Aldrich, 51280), N-acetylcysteine (200 μM, Sigma Aldrich, A7250), dithiothreitol (200 μM, Sigma Aldrich, 43816), glutathione (1 mM, Sigma Aldrich, G4251), or MitoTEMPO (20μM, Sigma Aldrich, SML0737). Cells were treated with 1 μM ISRIB (Sigma Aldrich, SML0843) or thapsigargin (Sigma Aldrich, T9033) for 24 h.

Mouse ECs—Mouse ECs were isolated for freshly harvested aortas and brains. Briefly, thoracic aorta and brain tissue were collected from eight-week-old *Cdh5-Cre*^{ERT2};*Rosa-LSL-tdTomato*;*Phgdh*$^{fl/wt}$ and *Cdh5-Cre*^{ERT2};*Rosa-LSL-tdTomato* mice that had received tamoxifen injection. The aortic rings were embedded in Matrigel-coated dishes and cultured for 5 d. After the rings were removed, the remaining cells were incubated with 2 U/ml Dispase II (Gibco, 17105–041) for 20 min at 37 °C. After centrifugation at 500 x g for 10 min, the cell pellets were washed with PBS and cultured in EC medium (ScienCell, 1001). Brain ECs were sorted from brain-derived single-cell suspensions based on tdTomato signal using a FACS Aria II cell sorter (BD Biosciences).

Cell lines—Human U251 glioma cells (Sigma Aldrich, 09063001), normal human astrocytes (Lonza, CC-2565), and Platinum-ECO cells (Cell Biolabs, RV-101) were cultured in DMEM medium supplemented with 5% FBS. All cells were maintained at 37 °C in a humidified atmosphere with 5% CO_2.

METHOD DETAILS

Preparation of glioma–conditioned medium—Human U251 glioma cells at about 90% confluence were exposed to hypoxia (1% O_2) in a humidified air atmosphere at 37°C for 24 hours. Culture medium were centrifuged at 5,000 × g for 30 minutes to remove cellular debris, and the supernatant collected.

Metabolite profiling and identification—Cell pellets were thawed on ice and metabolites were extracted using a modified Bligh-Dyer method [68,69]. Briefly, a methanol:chloroform (2:1) mixture was added to the cell pellets, followed by vortexing and sonication. After vortexing with added chloroform and water, organic and aqueous layers were separated by centrifugation. Aqueous layer was dried and re-dissolved in a mixture of 50:50 acetonitrile:water. The samples were centrifuged to remove fine particulates, and the supernatant was transferred to a LC-MS certified sample vial for ultraperformance liquid chromatography with 95:5 water:acetonitrile 20 mM ammonium acetate, pH 9 (solvent A) and 100% acetonitrile (solvent B), on a Waters Acquity UPLC coupled to a Waters TQD mass spectrometer (Waters). Mass spectrometry was performed on a QQQ quadrupole instrumentation (Xevo TQD or TQS-micro, Waters) operating using ion-switching. Data was acquired as multiple reaction monitoring's (MRM) to target specific metabolites along with validation either through standards or mass spectrometry databases. The entire set of triplicate sample injections were bracketed with a test mix of standard metabolites at the beginning and at the end of the run to evaluate instrument performance with respect to sensitivity and reproducible signal. The sample queue was randomized to remove bias. Mass spectroscopy data processing was performed using Waters TargetLynx software (version 4.1). Ion counts were exported from TargetLynx and subsequently processed in R (version 3.2). Quality control (QC) samples, which consisted of a pooled sample of all samples, were

injected at the beginning of the batch for LC column equilibration and every 6 injections during the analysis to account for instrumental drift. For every metabolic feature, a locally-weighted scatterplot smoothing function (LOESS) was fitted to the QC data, which was then used as a normalization factor for the samples as a function of run order [70]. OPLS-DA clustering of assayed samples was performed using the relative abundance of metabolites by R package ROPLS[71] (version 1.26.4) under R (version 4.0.5). Pathway analysis was conducted using Metabolites Enrichment Set Analysis [72].

Metabolic flux analysis—For [U-^{13}C]glucose labeling experiments, cells were cultured in glucose-, serine-, and glycine-free Endothelial Cell Growth Medium 2 (PromoCell, custom order) supplemented with 5% dialyzed FBS (Gibco, A3382001) and 5.5 mM glucose (Sigma Aldrich, G8270) for 24 h, and pretreated with 0.1% DMSO or 150 μM WQ-2201 (Biotechne, 6581) for 4 h. Cells were washed twice with PBS and then cultured in the same medium with 5.5 mM [U-^{13}C]glucose (Cambridge isotope laboratories, CLM-1396). Cells were treated with 0.1% DMSO or 150 μM WQ-2201 in the presence or absence of 1 mM glutathione (Sigma Aldrich, G4251) for 3 or 24 h. Treated cells were washed twice with ice-cold PBS and extracted with 400 μL of 80:20 acetonitrile:water over ice for 15 min. Cells were scraped off plates to be collected with supernatants, sonicated for 30 sec, then spun down at 15,000 RPM for 10 min. Supernatant (200 μL) was taken out for LC-MS/MS analysis. Quantitative LC-ESI-MS/MS analysis of [U-^{13}C]glucose-labeled cell extracts was performed using an Agilent 1290 UHPLC system equipped with an Agilent 6545 Q-TOF mass spectrometer using Agilent Profinder software (Agilent Technologies) [73].

Bulk RNAseq—2×10^6 ECs, isolated from human patients or normal brain, or treated with CRISPR sgRNA targeting PHGDH or control sequence, were lysed in 1 ml TRIzol (Thermo Fisher Scientific, 15596026), followed by RNA extraction according to the manufacturer's instructions. The isolated RNA was purified with RNeasy Plus Mini Kit (Qiagen). After a quality control step using RNA Nano assay chips with a 2100 Bioanalyzer (Agilent), a library was constructed using a Ribo-Zero protocol with TapeStation (Agilent) and subjected to deep sequencing (125 paired-end (PE); approximately 40 MB reads for each sample; Illumina HiSeq 2500 sequencer) at the Children's Hospital of Philadelphia. Reads were pseudo-aligned with Kallisto (version 0.46.1, b = 100) against the human genome (GRCh38 assembly) [74]. In R (version 4.0.5), transcripts were collapsed to genes using package tximport (version 1.22.0) [75], and then normalized and filtered by edgeR [76] (version 3.36.0) to generate counts per million mapped reads (CPM) for each gene. Genes with a CPM less than 0.1 in any sample were filtered and considered as genes with no or low expression. ECs isolated from human patent tumors or normal brain ECs, or normal brain ECs treated with or without glioma-conditioned medium [34], were sequenced on two separated runs and then integrated to eliminate the batch effect using the ComBat-seq method in R package sva[77] (version 3.42.0). Pathway over-representation analysis or gene set enrichment analysis was performed using R package clusterProfiler[78] (version 4.2.2) and gene sets from either 65 human metabolism modules in KEGG database[79] or Reactome pathway database [80].

Single-cell RNAseq—*Cdh5-Cre*^{ERT2};*Rosa-LSL-tdTomato* mice bearing RCAS-induced tumors were euthanized and perfused with PBS supplemented with EDTA. GBM tumors

and brain tissue from a healthy mouse were harvested and digested with collagenase-II (5 mg/ml, Invitrogen 17101–015) and DNase (1 mg/ml, Sigma Aldrich, D4527). Single-cell suspension was prepared after filtering using a mesh strainer with 100-μm pores. Cell samples were prepared and analyzed following a manufacturer's V3 library protocol (10x Genomics) and single-cell RNA-seq at the next-generation sequencing core at the University of Pennsylvania. Reads were aligned with CellRanger (10x Genomics, version 6.1.2) against customized mouse reference library (mm10) with tdTomato and firefly luciferase cDNA sequences to identity $tdTomato^+$ ECs and $fLuc^+$ tumor cells. The gene expression matrices that passed default quality control metrics were integrated by R package Seurat (version 4.0.6) using the sctransform (v2) method [81,82]. The downstream analysis was performed by Seurat and Monocle3 (version 1.0.0) [81]. For single-cell trajectory construction and pseudotime measurement, cells with EC or tumor lineage were subsetted from the original dataset and then further re-clustered and processed. Choice of root node was placed at one arbitrary end of the calculated trajectory, which was determined by the projected spatial distribution of expressing cells and the gradient of expression. For cell cycle analysis, the top 20 genes with the highest periodicity score for each cell cycle in tumor ECs described by Rohlenova et al. were used to score and classify the cell cycle [83]. For indexing the proliferation state of ECs, the top 20 markers described by Kalucka et al. for proliferating ECs were used [84].

Human GBM single-cell RNAseq meta-analysis—Single-cell RNAseq datasets from four different studies were collected (GSE84465, GSE103224, GSE131928, GSE117891) [85–88]. By analyzing the metadata available or the chromosomal aberrations in individual cells, all tumor cells were removed from each sample [89]. Only glioblastoma samples were used for this analysis. The datasets were integrated by the sctransform (v2) method [82]. R packages Seurat[81] (version 4.0.6) and Monocle3[90] (version 1.0.0) were used to analyze and visualize these datasets.

siRNA and CRISPR/sgRNA treatment—Cells were transfected with non-targeting control siRNA (Thermo Fisher, AM4611) or with siRNA targeting PHGDH (Dharmacon, L-009518–00-0005), ATF4 (Dharmacon, L-005125–00-0005) or NRF2 (Dharmacon, L-003755–00-0005) using RNAiMAX Lipofectamine (Invitrogen, 13778075) in serum-free Opti-MEM medium (Gibco, 31985–070) for 12 h, followed by incubation with serum-supplemented medium for 48 h. The sgRNA sequence (5'-CACCGGAGGCCGACAATGACTGCG −3') targeting PHGDH was subcloned into lentiCRISPRv2 puro vector (Addgene; 52961). Cells were transduced with the lentivirus expressing PHGDH sgRNA and Cas9, followed by cell selection by incubation with medium containing 2 μg/ml puromycin (Gibco, A1113803).

Cell viability assay—Calcein AM cell viability assay kit (Trevigen, 4892–010-K) was used to examine cell viability according to the protocol provided by the manufacturer. In brief, cells (5,000 cells/well) were seeded on black-well clear-bottom 96-well tissue culture plates (Thermo Scientific, 165305). After washing twice with 1X Calcein AM DW buffer, cells were incubated in 1X Calcein AM DW buffer containing Calcein AM (1 μM) for 30 minutes at 37 °C. Relative fluorescence unit (RFU) readings were obtained using a BioTek

Synergy H4 Hybrid Microplate Reader (BioTek) with 485/520 nm excitation/emission filters.

3D ex vivo EC outgrowth assay—Microvessels formed by normal brain endothelial cells pre-stained with CellTrace Far Red dye (Invitrogen, C34572) were co-cultured with U251 glioma cells in a 1:1 mixture with Matrigel (Corning, 356231) in 3D cell culture chips (AIM Biotech, DAX-1). Cells were seeded in the Matrigel by introducing ECs (1.5×10^6 cells/mL) and U251 cells (1.5×10^5 cells/mL). A 1:1 mixture of Endothelial Cell Growth Medium 2 (PromoCell, C-22211 and C-39211) and DMEM (Gibco, 10566032) supplemented with 5% FBS was added to the two lateral flow channels. 50 μL of the mixture was added into two connected ports and 70 μL was added to the other to maintain a transient flow across the Matrigel. Media was changed every 24 h for 5 days. Cells were imaged using an EVOS FL Auto 2 microscope (Invitrogen) with a far-red filter set. A 10-image z-stack was captured for each view, covering a depth of 100 μm. The acquired z-stacks were deconvoluted, reconstructed as 3D images, and analyzed by Imaris 9.8 (Oxford Instruments).

Biochemical assays—Total glutathione amount, GSH/GSSG ratio, relative NADH amount, NAD^+/NADH ratio and relative ATP amount were measured using GSH/GSSG-Glo™ Assay kit, NAD/NADH-Glo™ Assay kit, and CellTiter-Glo® Assay kit (Promega, V6611, G9071 and G7570), respectively, following the protocols provided by the manufacturer. Black-well clear-bottom 96-well tissue culture plates (Thermo Scientific, 165305) were seeded with cells (5,000 cells/well). Relative intensity of bioluminescence was acquired using a BioTek Synergy H4 Hybrid Microplate Reader (BioTek).

Immunoblot analysis—Cells were lysed with a NP-40 lysis buffer (Thermo Scientific, J60766-AP) containing protease inhibitor cocktail (Roche, 11697498001), followed by measurement of total protein concentration. A total of 40 μg protein of the lysates was resolved by 4–15% precast SDS-PAGE gel (Bio-Rad. 4561086). After transfer, PVDF membranes were blotted with anti-Vinculin (Atlas Antibodies, HPA002131), anti-PHGDH (Atlas Antibodies, HPA021241), anti-ATF4 (Cell Signaling, 11815), anti-NRF2 (Cell Signaling, 12721) antibody at 1:1,000 dilution. Proteins were detected with HRP-conjugated antibodies specific for rabbit IgG (Bio-Rad, 1706515), followed by ECL development (GE Healthcare, RPN2232). The developed signals were imaged by ChemiDoc MP system (Bio-Rad).

Real-time RT-PCR analysis—The total RNA was extracted and isolated with RNeasy Mini Kit (Qiagen, 74104) and subjected to reverse transcription with SuperScript III First-Strand Synthesis SuperMix (Invitrogen, 18080400). Real-time PCR was performed in a 20-μl reaction volume using Fast SYBR Green Master Mix (Applied Biosystems, 4385612) and PrimeTime pre-designed qPCR primers (Integrated DNA Technologies) for human HRPT1 (Hs.PT.58v.45621572), mouse B2m (Mm.PT.39a.22214835), human PHGDH (Hs.PT.58.2437570), and mouse Phgdh (Mm.PT.58.10927981).

ChIP-PCR—Chromatin immunoprecipitation (ChIP) assays were performed using an EZ-Magna ChIP Kit (Millipore,17–408) as previously described [34,91]. In brief, ECs were fixed with 1% formaldehyde. Cells were collected by scratching, lysed, and suspended in nuclear

buffer. Five cycles of continuous sonication for 10×2s were applied to break the chromatin into fragments between 100 and 500 base pairs. The samples were incubated with anti-ATF4 antibody (1:100, Cell Signaling, 11815) and magnetic beads overnight at 4 °C. Normal IgG was used as a negative control. Immunoprecipitants were separated using a magnetic rack and washed. DNA fragments were released by incubation with proteinase K at 62 °C for 2 h with continuous shaking and were isolated by filtration. Real-time PCR was performed in a 20-μl reaction volume using Fast SYBR Green Master Mix (Applied Biosystems; 4385612) and the following primer sets: #1-FP, 5'- AGTGCCTTGCACATTTACCC, #1-RP, 5'-CAAATCCCTGCCCGCTTTAT; #2-FP, 5'-GAGCTTTGGCTGAGATGGAGA, #2-RP, 5'-CTCAAACTCTCCGCGACTCC; #3-FP, 5'-CGGAGACCCAACCAGTCT, #3-RP, 5'-GGTACGTGTTTGCTGCCTTA; #4-FP, 5'-GCCCTCGTAAGGCAGCA, #4-RP, 5'-TCCTCCGAAGGCTCCCA; #5-FP, 5'-TCGTAAGGCAGCAAACACGTA, #5-RP, 5'-CGAAAGCACGGAGCAGTCTT).

Light sheet fluorescence imaging—Mouse GBM tissues were isolated and fixed in 4% paraformaldehyde overnight, then cleared according to a CLARITY protocol using the X-CLARITY Tissue Clearing System (Logos Biosystems) for 24 hours, as described previously [50]. Hypoxic areas were labeled with pimonidazole HCl (NPI, HP-200mg) injection before sacrifice and visualized by staining the tumor tissue with pimonidazole mouse FITC-mab (NPI, FITC MAb-1). CD3+ cells were labeled and visualized by staining the tumor tissue with anti-CD3ε antibody (Cell Signaling, 78588) and APC-conjugated F(ab')2-Goat anti-Rabbit IgG (H+L) antibody (Thermo Scientific, 31984). Cleared tissues were imaged using a Lightsheet Z.1 LSFM system (Zeiss) at the University of Pennsylvania Cell & Developmental Biology Microscopy Core. Obtained raw stack images were stitched and processed using Imaris 9.8 (Oxford Instruments).

CyTOF—Single-cell suspensions derived from freshly isolated tumors were prepared by mechanical dissociation with a gentleMACS Dissociator (Miltenyi Biotech) and enzymatic digestion with collagenase II (Invitrogen, 17101–015) and dispase II (Gibco, 17105–041). Cells were incubated with 25 μM cisplatin (Fluidigm, 201064), followed by staining at room temperature for 30 min with heavy metal-conjugated antibodies provided by cytometry by time of flight (CyTOF) core at the Penn Institute for Immunology [92]. Cells were fixed with 1.6% paraformaldehyde and stained with Cell-ID Intercalator-Ir (Fluidigm, 201192A) and analyzed using a CyTOF mass cytometer (Fluidigm), followed by analysis with R package CATALYST (version 1.18.1).

Flow cytometry—Single-cell suspensions derived from tumors were stained with fluorescence dye-conjugated antibodies against CD3 (1 : 100, BioLegend, 100233), CD45 (1 : 100, eBioscience, 48–0451-82), CD8a (1 : 100, BioLegend, 100706), CD4 (1 : 100, BioLegend, 100411), Foxp3 (1 : 100, BioLegend, 126407), NK1.1 (1 : 100, BioLegend, 108707), F4/80 (1 : 200, BioLegend, 123107), CD11b (1 : 200, BioLegend, 101228), CD11c (1 : 200, eBioscience, 17–0114-81), CD45R/B220 (1 : 100, BioLegend, 103228), or control IgG. For BrdU assay, cells were labeled with BrdU using a FITC-BrdU flow kit (BD Pharmingen 559619). GBM tumor ECs were pulsed in 10 μM BrdU for 45 min. Cells

were analyzed using FACSCanto II flow cytometers (BD Biosciences) and FlowJo software (V10).

Mouse T cell isolation and transduction—The tdTomato-T2A-nLuc sequence was subcloned into the pMMLV vector (Vector builder). Egfrviii-specific CAR with 139 scFv was generated with mouse CD8 trans-membrane, CD28, 4–1BB and CD3ζ intracellular regions in an MSGV1 retroviral vector as described previously [50]. Retrovirus was generated by transfection with plasmids encoding tdTomato-T2A-nLuc and Egfrviii or control CAR (provided by Steven Albelda and Michael Leibowitz, University of Pennsylvania) with Platinum-ECO cells (Cell Biolabs, RV-101) using Lipofectamine 3000 Transfection Reagent (Life Technologies; L3000001). The retroviral supernatant was collected and filtrated using sterilized filters with 0.45-μm pores. Mouse T cells were isolated from mouse spleens using an EasySep Mouse T Cell Isolation Kit (Stemcell technologies, 19851) and stimulated with anti-mouse CD3ε antibody (1 μg/ml; eBioscience, 14–0031), anti-mouse CD28 antibody (0.5 μg/ml; eBioscience, 14–0281), and rhIL-2 (100 U/ml, Peprotech, 200–02) in RPMI 1640 (Gibco, 72400120) supplemented with 10% FBS for 36 h, followed by spinfection/centrifugation at 2000 x g at 30°C for 90 min with the retroviral supernatant in plates coated with RetroNectin (20 μg/ml, Takara, T100A). T cells were cultured in 10% FBS RPMI 1640 medium supplemented with 100 U/ml rhIL-2 for 3 days. 24 to 48 hours after the spinfection, transduced T cells were stained for surface Egfrviii CAR expression using a goat anti-human IgG $F(ab')_2$ fragment (Jackson ImmunoResearch, 109–136-097). Cells were analyzed using a FACSCanto II flow cytometer (BD Biosciences) with FlowJo software (v10).

QUANTIFICATION AND STATISTICAL ANALYSIS

Statistical analyses were performed with Prism software (GraphPad 9). Statistical significance was evaluated with two-tailed unpaired Student's and Mann-Whitney *t* tests for comparing two groups and with ANOVA tests for comparing more than two groups. Survival analysis was performed with Mantel–Cox Log-rank tests. $P < 0.05$ was considered to represent a statistically significant difference.

Supplementary Material

Refer to Web version on PubMed Central for supplementary material.

ACKNOWLEDGMENTS

We are grateful to Eric Holland for providing the RCAS-PDGF GBM model, to Jonathan Schug for RNA sequencing, to Leonel Joannas for transgenic mouse generation, to Itzhak Nissim for metabolite tracing analysis, to Aalim Weljie for helps with metabolic assays, to Andrea Stout for helps with microscopy, to Yiyun Chen for helps with data visualization, and to Sandra Ryeom and Zoltan Arany for helpful discussion. This work was supported in part by National Institutes of Health grants R01NS094533 (to Y.F.), R01NS106108 (to Y.F.), R01CA241501 (to Y.F.), and R01HL155198 (to Y.F. and Y.G.), American Cancer Society Research Scholar Grant RSG-20-036-01 (to J.Y.), and American Heart Association Predoctoral Fellowship (to D.Z.). The graphic abstract was created with BioRender.com.

INCLUSION AND DIVERSITY

We support inclusive, diverse, and equitable conduct of research.

REFERENCES

1. Carmeliet P, and Jain RK (2011). Principles and mechanisms of vessel normalization for cancer and other angiogenic diseases. Nat Rev Drug Discov 10, 417–427. nrd3455 [pii]10.1038/nrd3455. [PubMed: 21629292]
2. Weis SM, and Cheresh DA (2011). Tumor angiogenesis: molecular pathways and therapeutic targets. Nat Med 17, 1359–1370. nm.2537 [pii]10.1038/nm.2537. [PubMed: 22064426]
3. Hanahan D, and Weinberg RA (2011). Hallmarks of cancer: the next generation. Cell 144, 646–674. S0092–8674(11)00127–9 [pii]10.1016/j.cell.2011.02.013. [PubMed: 21376230]
4. Lanitis E, Irving M, and Coukos G. (2015). Targeting the tumor vasculature to enhance T cell activity. Curr Opin Immunol 33, 55–63. 10.1016/j.coi.2015.01.011. [PubMed: 25665467]
5. Wang Q, He Z, Huang M, Liu T, Wang Y, Xu H, Duan H, Ma P, Zhang L, Zamvil SS, et al. (2018). Vascular niche IL-6 induces alternative macrophage activation in glioblastoma through HIF-2alpha. Nat Commun 9, 559. 10.1038/s41467-018-03050-0. [PubMed: 29422647]
6. Huang Y, Kim BYS, Chan CK, Hahn SM, Weissman IL, and Jiang W. (2018). Improving immune-vascular crosstalk for cancer immunotherapy. Nat Rev Immunol 18, 195–203. 10.1038/nri.2017.145. [PubMed: 29332937]
7. Klein D. (2018). The Tumor Vascular Endothelium as Decision Maker in Cancer Therapy. Front Oncol 8, 367. 10.3389/fonc.2018.00367. [PubMed: 30250827]
8. Zheng X, Fang Z, Liu X, Deng S, Zhou P, Wang X, Zhang C, Yin R, Hu H, Chen X, et al. (2018). Increased vessel perfusion predicts the efficacy of immune checkpoint blockade. J Clin Invest 128, 2104–2115. 10.1172/JCI96582. [PubMed: 29664018]
9. Schaaf MB, Garg AD, and Agostinis P. (2018). Defining the role of the tumor vasculature in antitumor immunity and immunotherapy. Cell Death Dis 9, 115. 10.1038/s41419-017-0061-0. [PubMed: 29371595]
10. Batchelor TT., Sorensen AG., di Tomaso E., Zhang WT., Duda DG., Cohen KS., Kozak KR., Cahill DP., Chen PJ., Zhu M., et al. . (2007). AZD2171, a pan-VEGF receptor tyrosine kinase inhibitor, normalizes tumor vasculature and alleviates edema in glioblastoma patients. Cancer Cell 11, 83–95. S1535–6108(06)00370–9 [pii]10.1016/j.ccr.2006.11.021. [PubMed: 17222792]
11. Jain RK (2014). Antiangiogenesis strategies revisited: from starving tumors to alleviating hypoxia. Cancer Cell 26, 605–622. 10.1016/j.ccell.2014.10.006. [PubMed: 25517747]
12. Gilbert MR, Dignam JJ, Armstrong TS, Wefel JS, Blumenthal DT, Vogelbaum MA, Colman H, Chakravarti A, Pugh S, Won M, et al. (2014). A randomized trial of bevacizumab for newly diagnosed glioblastoma. N Engl J Med 370, 699–708. 10.1056/NEJMoa1308573. [PubMed: 24552317]
13. De Bock K, Georgiadou M, Schoors S, Kuchnio A, Wong BW, Cantelmo AR, Quaegebeur A, Ghesquiere B, Cauwenberghs S, Eelen G, et al. (2013). Role of PFKFB3-driven glycolysis in vessel sprouting. Cell 154, 651–663. 10.1016/j.cell.2013.06.037. [PubMed: 23911327]
14. Zahalka AH, Arnal-Estape A, Maryanovich M, Nakahara F, Cruz CD, Finley LWS, and Frenette PS (2017). Adrenergic nerves activate an angio-metabolic switch in prostate cancer. Science 358, 321–326. 10.1126/science.aah5072. [PubMed: 29051371]
15. Potente M, and Carmeliet P. (2017). The Link Between Angiogenesis and Endothelial Metabolism. Annu Rev Physiol 79, 43–66. 10.1146/annurev-physiol-021115-105134. [PubMed: 27992732]
16. Schoors S, Bruning U, Missiaen R, Queiroz KC, Borgers G, Elia I, Zecchin A, Cantelmo AR, Christen S, Goveia J, et al. (2015). Fatty acid carbon is essential for dNTP synthesis in endothelial cells. Nature 520, 192–197. 10.1038/nature14362. [PubMed: 25830893]
17. Bruning U, Morales-Rodriguez F, Kalucka J, Goveia J, Taverna F, Queiroz KCS, Dubois C, Cantelmo AR, Chen R, Loroch S, et al. (2018). Impairment of Angiogenesis by Fatty Acid Synthase Inhibition Involves mTOR Malonylation. Cell Metab 28, 866–880 e815. 10.1016/j.cmet.2018.07.019. [PubMed: 30146486]
18. Kim B, Jang C, Dharaneeswaran H, Li J, Bhide M, Yang S, Li K, and Arany Z. (2018). Endothelial pyruvate kinase M2 maintains vascular integrity. J Clin Invest 128, 4543–4556. 10.1172/JCI120912. [PubMed: 30222136]

19. Diebold LP, Gil HJ, Gao P, Martinez CA, Weinberg SE, and Chandel NS (2019). Mitochondrial complex III is necessary for endothelial cell proliferation during angiogenesis. Nat Metab 1, 158–171. 10.1038/s42255-018-0011-x. [PubMed: 31106291]
20. Kim B, Li J, Jang C, and Arany Z. (2017). Glutamine fuels proliferation but not migration of endothelial cells. EMBO J 36, 2321–2333. 10.15252/embj.201796436. [PubMed: 28659379]
21. Li X, Sun X, and Carmeliet P. (2019). Hallmarks of Endothelial Cell Metabolism in Health and Disease. Cell Metab 30, 414–433. 10.1016/j.cmet.2019.08.011. [PubMed: 31484054]
22. Xiong J, Kawagishi H, Yan Y, Liu J, Wells QS, Edmunds LR, Fergusson MM, Yu ZX, Rovira II, Brittain EL, et al. (2018). A Metabolic Basis for Endothelial-to-Mesenchymal Transition. Mol Cell 69, 689–698 e687. 10.1016/j.molcel.2018.01.010. [PubMed: 29429925]
23. Cantelmo AR, Pircher A, Kalucka J, and Carmeliet P. (2017). Vessel pruning or healing: endothelial metabolism as a novel target? Expert Opin Ther Targets 21, 239–247. 10.1080/14728222.2017.1282465. [PubMed: 28081641]
24. Stupp R., Mason WP., van den Bent MJ., Weller M., Fisher B., Taphoorn MJ., Belanger K., Brandes AA., Marosi C., Bogdahn U., et al. . (2005). Radiotherapy plus concomitant and adjuvant temozolomide for glioblastoma. N Engl J Med 352, 987–996. 10.1056/NEJMoa043330. [PubMed: 15758009]
25. Huse JT, and Holland EC (2010). Targeting brain cancer: advances in the molecular pathology of malignant glioma and medulloblastoma. Nat Rev Cancer 10, 319–331. nrc2818 [pii]10.1038/nrc2818. [PubMed: 20414201]
26. Kim KJ, Li B, Winer J, Armanini M, Gillett N, Phillips HS, and Ferrara N. (1993). Inhibition of vascular endothelial growth factor-induced angiogenesis suppresses tumour growth in vivo. Nature 362, 841–844. 10.1038/362841a0. [PubMed: 7683111]
27. Friedman HS, Prados MD, Wen PY, Mikkelsen T, Schiff D, Abrey LE, Yung WK, Paleologos N, Nicholas MK, Jensen R, et al. (2009). Bevacizumab alone and in combination with irinotecan in recurrent glioblastoma. J Clin Oncol 27, 4733–4740. JCO.2008.19.8721 [pii]10.1200/JCO.2008.19.8721. [PubMed: 19720927]
28. Chinot OL, Wick W, Mason W, Henriksson R, Saran F, Nishikawa R, Carpentier AF, Hoang-Xuan K, Kavan P, Cernea D, et al. (2014). Bevacizumab plus radiotherapy-temozolomide for newly diagnosed glioblastoma. N Engl J Med 370, 709–722. 10.1056/NEJMoa1308345. [PubMed: 24552318]
29. Zhao J, Chen AX, Gartrell RD, Silverman AM, Aparicio L, Chu T, Bordbar D, Shan D, Samanamud J, Mahajan A, et al. (2019). Immune and genomic correlates of response to anti-PD-1 immunotherapy in glioblastoma. Nat Med 25, 462–469. 10.1038/s41591-019-0349-y. [PubMed: 30742119]
30. O'Rourke DM, Nasrallah MP, Desai A, Melenhorst JJ, Mansfield K, Morrissette JJD, Martinez-Lage M, Brem S, Maloney E, Shen A, et al. (2017). A single dose of peripherally infused EGFRvIII-directed CAR T cells mediates antigen loss and induces adaptive resistance in patients with recurrent glioblastoma. Sci Transl Med 9. 10.1126/scitranslmed.aaa0984.
31. Xie YJ, Dougan M, Jailkhani N, Ingram J, Fang T, Kummer L, Momin N, Pishesha N, Rickelt S, Hynes RO, and Ploegh H. (2019). Nanobody-based CAR T cells that target the tumor microenvironment inhibit the growth of solid tumors in immunocompetent mice. Proc Natl Acad Sci U S A 116, 7624–7631. 10.1073/pnas.1817147116. [PubMed: 30936321]
32. Datta M, Coussens LM, Nishikawa H, Hodi FS, and Jain RK (2019). Reprogramming the Tumor Microenvironment to Improve Immunotherapy: Emerging Strategies and Combination Therapies. Am Soc Clin Oncol Educ Book 39, 165–174. 10.1200/EDBK_237987. [PubMed: 31099649]
33. Huang M, Liu T, Ma P, Mitteer RA Jr., Zhang Z, Kim HJ, Yeo E, Zhang D, Cai P, Li C, et al. (2016). c-Met-mediated endothelial plasticity drives aberrant vascularization and chemoresistance in glioblastoma. J Clin Invest 126, 1801–1814. 10.1172/JCI84876. [PubMed: 27043280]
34. Liu T, Ma W, Xu H, Huang M, Zhang D, He Z, Zhang L, Brem S, O'Rourke DM, Gong Y, et al. (2018). PDGF-mediated mesenchymal transformation renders endothelial resistance to anti-VEGF treatment in glioblastoma. Nat Commun 9, 3439. 10.1038/s41467-018-05982-z. [PubMed: 30150753]

35. Possemato R, Marks KM, Shaul YD, Pacold ME, Kim D, Birsoy K, Sethumadhavan S, Woo HK, Jang HG, Jha AK, et al. (2011). Functional genomics reveal that the serine synthesis pathway is essential in breast cancer. Nature 476, 346–350. 10.1038/nature10350. [PubMed: 21760589]
36. Zeisberg EM, Potenta S, Xie L, Zeisberg M, and Kalluri R. (2007). Discovery of endothelial to mesenchymal transition as a source for carcinoma-associated fibroblasts. Cancer Res 67, 10123–10128. 10.1158/0008-5472.CAN-07-3127. [PubMed: 17974953]
37. Wang Q, Liberti MV, Liu P, Deng X, Liu Y, Locasale JW, and Lai L. (2017). Rational Design of Selective Allosteric Inhibitors of PHGDH and Serine Synthesis with Anti-tumor Activity. Cell Chem Biol 24, 55–65. 10.1016/j.chembiol.2016.11.013. [PubMed: 28042046]
38. Yang M, and Vousden KH (2016). Serine and one-carbon metabolism in cancer. Nat Rev Cancer 16, 650–662. 10.1038/nrc.2016.81. [PubMed: 27634448]
39. Vandekeere S., Dubois C., Kalucka J., Sullivan MR., Garcia-Caballero M., Goveia J., Chen R., Diehl FF., Bar-Lev L., Souffreau J., et al. . (2018). Serine Synthesis via PHGDH Is Essential for Heme Production in Endothelial Cells. Cell Metab 28, 573–587 e513. 10.1016/j.cmet.2018.06.009. [PubMed: 30017355]
40. Friedrich M, Sankowski R, Bunse L, Kilian M, Green E, Ramallo Guevara C, Pusch S, Poschet G, Sanghvi K, Hahn M, et al. (2021). Tryptophan metabolism drives dynamic immunosuppressive myeloid states in IDH-mutant gliomas. Nat Cancer 2, 723–740. 10.1038/s43018-021-00201-z. [PubMed: 35121943]
41. Bunse L, Pusch S, Bunse T, Sahm F, Sanghvi K, Friedrich M, Alansary D, Sonner JK, Green E, Deumelandt K, et al. (2018). Suppression of antitumor T cell immunity by the oncometabolite (R)-2-hydroxyglutarate. Nat Med 24, 1192–1203. 10.1038/s41591-018-0095-6. [PubMed: 29988124]
42. Fan J, Teng X, Liu L, Mattaini KR, Looper RE, Vander Heiden MG, and Rabinowitz JD (2015). Human phosphoglycerate dehydrogenase produces the oncometabolite D-2-hydroxyglutarate. ACS Chem Biol 10, 510–516. 10.1021/cb500683c. [PubMed: 25406093]
43. Reid MA, Allen AE, Liu S, Liberti MV, Liu P, Liu X, Dai Z, Gao X, Wang Q, Liu Y, et al. (2018). Serine synthesis through PHGDH coordinates nucleotide levels by maintaining central carbon metabolism. Nat Commun 9, 5442. 10.1038/s41467-018-07868-6. [PubMed: 30575741]
44. Verginadis II, Avgousti H, Monslow J, Skoufos G, Chinga F, Kim K, Leli NM, Karagounis IV, Bell BI, Velalopoulou A, et al. (2022). A stromal Integrated Stress Response activates perivascular cancer-associated fibroblasts to drive angiogenesis and tumour progression. Nat Cell Biol 24, 940–953. 10.1038/s41556-022-00918-8. [PubMed: 35654839]
45. He CH, Gong P, Hu B, Stewart D, Choi ME, Choi AM, and Alam J. (2001). Identification of activating transcription factor 4 (ATF4) as an Nrf2-interacting protein. Implication for heme oxygenase-1 gene regulation. J Biol Chem 276, 20858–20865. 10.1074/jbc.M101198200. [PubMed: 11274184]
46. DeNicola GM, Chen PH, Mullarky E, Sudderth JA, Hu Z, Wu D, Tang H, Xie Y, Asara JM, Huffman KE, et al. (2015). NRF2 regulates serine biosynthesis in non-small cell lung cancer. Nat Genet 47, 1475–1481. 10.1038/ng.3421. [PubMed: 26482881]
47. Hatfield SM, Kjaergaard J, Lukashev D, Schreiber TH, Belikoff B, Abbott R, Sethumadhavan S, Philbrook P, Ko K, Cannici R, et al. (2015). Immunological mechanisms of the antitumor effects of supplemental oxygenation. Sci Transl Med 7, 277ra230. 10.1126/scitranslmed.aaa1260.
48. Tyrakis PA, Palazon A, Macias D, Lee KL, Phan AT, Velica P, You J, Chia GS, Sim J, Doedens A, et al. (2016). S-2-hydroxyglutarate regulates CD8(+) T-lymphocyte fate. Nature 540, 236–241. 10.1038/nature20165. [PubMed: 27798602]
49. Sampson JH, Choi BD, Sanchez-Perez L, Suryadevara CM, Snyder DJ, Flores CT, Schmittling RJ, Nair SK, Reap EA, Norberg PK, et al. (2014). EGFRvIII mCAR-modified T-cell therapy cures mice with established intracerebral glioma and generates host immunity against tumor-antigen loss. Clin Cancer Res 20, 972–984. 10.1158/1078-0432.CCR-13-0709. [PubMed: 24352643]
50. Ma W, Wang Y, Zhang R, Yang F, Zhang D, Huang M, Zhang L, Dorsey JF, Binder ZA, O'Rourke DM, et al. (2021). Targeting PAK4 to reprogram vascular microenvironment and improve CAR T immunotherapy for glioblastoma. Nature Cancer 2, 83–97. [PubMed: 35121889]

51. Sampson JH, Maus MV, and June CH (2017). Immunotherapy for Brain Tumors. J Clin Oncol 35, 2450–2456. 10.1200/JCO.2017.72.8089. [PubMed: 28640704]
52. Bovenberg MS, Degeling MH, and Tannous BA (2013). Cell-based immunotherapy against gliomas: from bench to bedside. Mol Ther 21, 1297–1305. 10.1038/mt.2013.80. [PubMed: 23648695]
53. June CH (2007). Principles of adoptive T cell cancer therapy. J Clin Invest 117, 1204–1212. 10.1172/JCI31446. [PubMed: 17476350]
54. Fan Y. (2019). Vascular Detransformation for Cancer Therapy. Trends Cancer 5, 460–463. 10.1016/j.trecan.2019.05.007. [PubMed: 31421902]
55. Schoors S, De Bock K, Cantelmo AR, Georgiadou M, Ghesquiere B, Cauwenberghs S, Kuchnio A, Wong BW, Quaegebeur A, Goveia J, et al. (2014). Partial and transient reduction of glycolysis by PFKFB3 blockade reduces pathological angiogenesis. Cell Metab 19, 37–48. 10.1016/j.cmet.2013.11.008. [PubMed: 24332967]
56. Cantelmo AR., Conradi LC., Brajic A., Goveia J., Kalucka J., Pircher A., Chaturvedi P., Hol J., Thienpont B., Teuwen LA., et al. . (2016). Inhibition of the Glycolytic Activator PFKFB3 in Endothelium Induces Tumor Vessel Normalization, Impairs Metastasis, and Improves Chemotherapy. Cancer Cell 30, 968–985. 10.1016/j.ccell.2016.10.006. [PubMed: 27866851]
57. Haas R, Smith J, Rocher-Ros V, Nadkarni S, Montero-Melendez T, D'Acquisto F, Bland EJ, Bombardieri M, Pitzalis C, Perretti M, et al. (2015). Lactate Regulates Metabolic and Pro-inflammatory Circuits in Control of T Cell Migration and Effector Functions. PLoS Biol 13, e1002202. 10.1371/journal.pbio.1002202.
58. Newman AC, and Maddocks ODK (2017). Serine and Functional Metabolites in Cancer. Trends Cell Biol 27, 645–657. 10.1016/j.tcb.2017.05.001. [PubMed: 28601431]
59. Ye J, Fan J, Venneti S, Wan YW, Pawel BR, Zhang J, Finley LW, Lu C, Lindsten T, Cross JR, et al. (2014). Serine catabolism regulates mitochondrial redox control during hypoxia. Cancer Discov 4, 1406–1417. 10.1158/2159-8290.CD-14-0250. [PubMed: 25186948]
60. Reina-Campos M, Diaz-Meco MT, and Moscat J. (2020). The complexity of the serine glycine one-carbon pathway in cancer. J Cell Biol 219. 10.1083/jcb.201907022.
61. Amelio I, Cutruzzola F, Antonov A, Agostini M, and Melino G. (2014). Serine and glycine metabolism in cancer. Trends Biochem Sci 39, 191–198. 10.1016/j.tibs.2014.02.004. [PubMed: 24657017]
62. Maddocks ODK, Athineos D, Cheung EC, Lee P, Zhang T, van den Broek NJF, Mackay GM, Labuschagne CF, Gay D, Kruiswijk F, et al. (2017). Modulating the therapeutic response of tumours to dietary serine and glycine starvation. Nature 544, 372–376. 10.1038/nature22056. [PubMed: 28425994]
63. Chaneton B, Hillmann P, Zheng L, Martin ACL, Maddocks ODK, Chokkathukalam A, Coyle JE, Jankevics A, Holding FP, Vousden KH, et al. (2012). Serine is a natural ligand and allosteric activator of pyruvate kinase M2. Nature 491, 458–462. 10.1038/nature11540. [PubMed: 23064226]
64. Sullivan MR, Mattaini KR, Dennstedt EA, Nguyen AA, Sivanand S, Reilly MF, Meeth K, Muir A, Darnell AM, Bosenberg MW, et al. (2019). Increased Serine Synthesis Provides an Advantage for Tumors Arising in Tissues Where Serine Levels Are Limiting. Cell Metab 29, 1410–1421 e1414. 10.1016/j.cmet.2019.02.015. [PubMed: 30905671]
65. Murphy JP, Giacomantonio MA, Paulo JA, Everley RA, Kennedy BE, Pathak GP, Clements DR, Kim Y, Dai C, Sharif T, et al. (2018). The NAD(+) Salvage Pathway Supports PHGDH-Driven Serine Biosynthesis. Cell Rep 24, 2381–2391 e2385. 10.1016/j.celrep.2018.07.086. [PubMed: 30157431]
66. Diehl FF, Lewis CA, Fiske BP, and Vander Heiden MG (2019). Cellular redox state constrains serine synthesis and nucleotide production to impact cell proliferation. Nat Metab 1, 861–867. 10.1038/s42255-019-0108-x. [PubMed: 31598584]
67. Locasale JW, Grassian AR, Melman T, Lyssiotis CA, Mattaini KR, Bass AJ, Heffron G, Metallo CM, Muranen T, Sharfi H, et al. (2011). Phosphoglycerate dehydrogenase diverts glycolytic flux and contributes to oncogenesis. Nat Genet 43, 869–874. 10.1038/ng.890. [PubMed: 21804546]

68. Bligh EG, and Dyer WJ (1959). A rapid method of total lipid extraction and purification. Can J Biochem Physiol 37, 911–917. 10.1139/o59-099. [PubMed: 13671378]
69. Tambellini NP, Zaremberg V, Turner RJ, and Weljie AM (2013). Evaluation of extraction protocols for simultaneous polar and non-polar yeast metabolite analysis using multivariate projection methods. Metabolites 3, 592–605. 10.3390/metabo3030592. [PubMed: 24958140]
70. Dunn WB., Broadhurst D., Begley P., Zelena E., Francis-McIntyre S., Anderson N., Brown M., Knowles JD., Halsall A., Haselden JN., et al. . (2011). Procedures for large-scale metabolic profiling of serum and plasma using gas chromatography and liquid chromatography coupled to mass spectrometry. Nat Protoc 6, 1060–1083. 10.1038/nprot.2011.335. [PubMed: 21720319]
71. Thevenot EA, Roux A, Xu Y, Ezan E, and Junot C. (2015). Analysis of the Human Adult Urinary Metabolome Variations with Age, Body Mass Index, and Gender by Implementing a Comprehensive Workflow for Univariate and OPLS Statistical Analyses. J Proteome Res 14, 3322–3335. 10.1021/acs.jproteome.5b00354. [PubMed: 26088811]
72. Xia J, and Wishart DS (2010). MSEA: a web-based tool to identify biologically meaningful patterns in quantitative metabolomic data. Nucleic Acids Res 38, W71–77. 10.1093/nar/gkq329. [PubMed: 20457745]
73. Li AM, Ducker GS, Li Y, Seoane JA, Xiao Y, Melemenidis S, Zhou Y, Liu L, Vanharanta S, Graves EE, et al. (2020). Metabolic Profiling Reveals a Dependency of Human Metastatic Breast Cancer on Mitochondrial Serine and One-Carbon Unit Metabolism. Mol Cancer Res 18, 599–611. 10.1158/1541-7786.MCR-19-0606. [PubMed: 31941752]
74. Bray NL, Pimentel H, Melsted P, and Pachter L. (2016). Near-optimal probabilistic RNA-seq quantification. Nat Biotechnol 34, 525–527. 10.1038/nbt.3519. [PubMed: 27043002]
75. Soneson C, Love MI, and Robinson MD (2015). Differential analyses for RNA-seq: transcript-level estimates improve gene-level inferences. F1000Res 4, 1521. 10.12688/f1000research.7563.2. [PubMed: 26925227]
76. Robinson MD, McCarthy DJ, and Smyth GK (2010). edgeR: a Bioconductor package for differential expression analysis of digital gene expression data. Bioinformatics 26, 139–140. 10.1093/bioinformatics/btp616. [PubMed: 19910308]
77. Zhang Y, Parmigiani G, and Johnson WE (2020). ComBat-seq: batch effect adjustment for RNA-seq count data. NAR Genom Bioinform 2, lqaa078. 10.1093/nargab/lqaa078.
78. Wu T, Hu E, Xu S, Chen M, Guo P, Dai Z, Feng T, Zhou L, Tang W, Zhan L, et al. (2021). clusterProfiler 4.0: A universal enrichment tool for interpreting omics data. Innovation (N Y) 2, 100141. 10.1016/j.xinn.2021.100141.
79. Kanehisa M, and Goto S. (2000). KEGG: kyoto encyclopedia of genes and genomes. Nucleic Acids Res 28, 27–30. 10.1093/nar/28.1.27. [PubMed: 10592173]
80. Gillespie M, Jassal B, Stephan R, Milacic M, Rothfels K, Senff-Ribeiro A, Griss J, Sevilla C, Matthews L, Gong C, et al. (2022). The reactome pathway knowledgebase 2022. Nucleic Acids Res 50, D687–D692. 10.1093/nar/gkab1028. [PubMed: 34788843]
81. Hao Y, Hao S, Andersen-Nissen E, Mauck WM 3rd, Zheng S, Butler A, Lee MJ, Wilk AJ, Darby C, Zager M, et al. (2021). Integrated analysis of multimodal single-cell data. Cell 184, 3573–3587 e3529. 10.1016/j.cell.2021.04.048. [PubMed: 34062119]
82. Hafemeister C, and Satija R. (2019). Normalization and variance stabilization of single-cell RNA-seq data using regularized negative binomial regression. Genome Biol 20, 296. 10.1186/s13059-019-1874-1. [PubMed: 31870423]
83. Rohlenova K, Goveia J, Garcia-Caballero M, Subramanian A, Kalucka J, Treps L, Falkenberg KD, de Rooij L, Zheng Y, Lin L, et al. (2020). Single-Cell RNA Sequencing Maps Endothelial Metabolic Plasticity in Pathological Angiogenesis. Cell Metab 31, 862–877 e814. 10.1016/j.cmet.2020.03.009. [PubMed: 32268117]
84. Kalucka J, de Rooij L, Goveia J, Rohlenova K, Dumas SJ, Meta E, Conchinha NV, Taverna F, Teuwen LA, Veys K, et al. (2020). Single-Cell Transcriptome Atlas of Murine Endothelial Cells. Cell 180, 764–779 e720. 10.1016/j.cell.2020.01.015. [PubMed: 32059779]
85. Darmanis S., Sloan SA., Croote D., Mignardi M., Chernikova S., Samghababi P., Zhang Y., Neff N., Kowarsky M., Caneda C., et al. . (2017). Single-Cell RNA-Seq Analysis of Infiltrating

Neoplastic Cells at the Migrating Front of Human Glioblastoma. Cell Rep 21, 1399–1410. 10.1016/j.celrep.2017.10.030. [PubMed: 29091775]

86. Yuan J, Levitin HM, Frattini V, Bush EC, Boyett DM, Samanamud J, Ceccarelli M, Dovas A, Zanazzi G, Canoll P, et al. (2018). Single-cell transcriptome analysis of lineage diversity in high-grade glioma. Genome Med 10, 57. 10.1186/s13073-018-0567-9. [PubMed: 30041684]
87. Neftel C, Laffy J, Filbin MG, Hara T, Shore ME, Rahme GJ, Richman AR, Silverbush D, Shaw ML, Hebert CM, et al. (2019). An Integrative Model of Cellular States, Plasticity, and Genetics for Glioblastoma. Cell 178, 835–849 e821. 10.1016/j.cell.2019.06.024. [PubMed: 31327527]
88. Yu K, Hu Y, Wu F, Guo Q, Qian Z, Hu W, Chen J, Wang K, Fan X, Wu X, et al. (2020). Surveying brain tumor heterogeneity by single-cell RNA-sequencing of multi-sector biopsies. Natl Sci Rev 7, 1306–1318. 10.1093/nsr/nwaa099. [PubMed: 34692159]
89. Caruso FP, Garofano L, D'Angelo F, Yu K, Tang F, Yuan J, Zhang J, Cerulo L, Pagnotta SM, Bedognetti D, et al. (2020). A map of tumor-host interactions in glioma at single-cell resolution. Gigascience 9. 10.1093/gigascience/giaa109.
90. Trapnell C, Cacchiarelli D, Grimsby J, Pokharel P, Li S, Morse M, Lennon NJ, Livak KJ, Mikkelsen TS, and Rinn JL (2014). The dynamics and regulators of cell fate decisions are revealed by pseudotemporal ordering of single cells. Nat Biotechnol 32, 381–386. 10.1038/nbt.2859. [PubMed: 24658644]
91. Huang M, Zhang D, Wu JY, Xing K, Yeo E, Li C, Zhang L, Holland E, Yao L, Qin L, et al. (2020). Wnt-mediated endothelial transformation into mesenchymal stem cell-like cells induces chemoresistance in glioblastoma. Sci Transl Med 12. 10.1126/scitranslmed.aay7522.
92. Yang F, He Z, Duan H, Zhang D, Li J, Yang H, Dorsey JF, Zou W, Ali Nabavizadeh S, Bagley SJ, et al. (2021). Synergistic immunotherapy of glioblastoma by dual targeting of IL-6 and CD40. Nature Communications 12, 3424. 10.1038/s41467-021-23832-3.

Highlights

- PHGDH-mediated serine metabolism is preferentially altered in tumor-associated ECs.
- ATF4-mediated PHGDH expression enhances glycolysis and nucleotide synthesis in ECs.
- Genetic ablation of PHGDH prunes tumor vasculature and promotes T cell infiltration.
- PHGDH inhibition overcome GBM resistance to CAR T cell therapy.

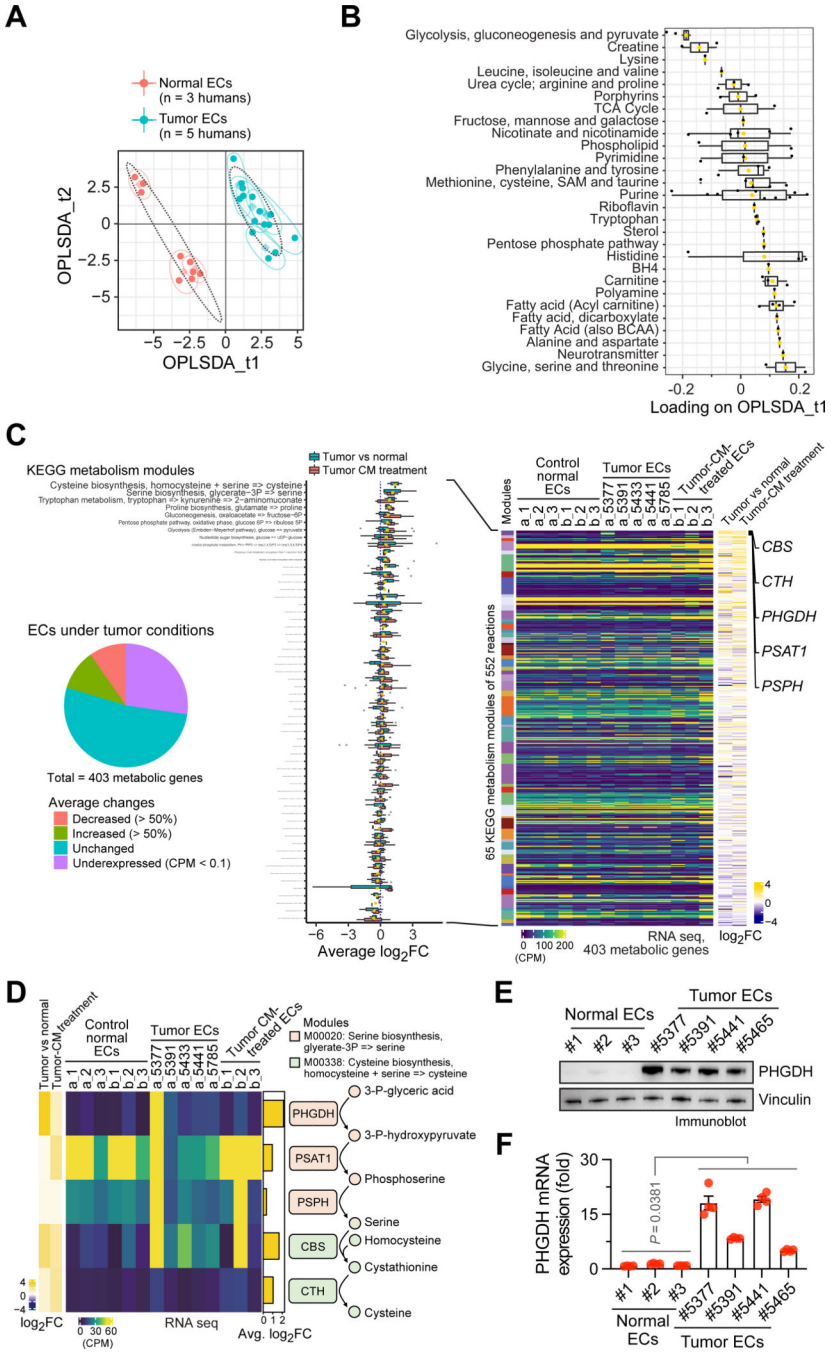

Figure 1. Metabolomic and transcriptomic analyses identify altered serine metabolism and PHGDH expression in tumor ECs.

Human ECs were isolated from normal brains or GBM tumors.

(A,B) Cellular metabolites were analyzed by LC-MS (n = 3–5 human samples, pooled from three assays).

(A) Dimensionality reduction analysis. Ellipse lines with center diamonds indicate 95% Cl ranges with means.

(B) Pathway analysis of changed metabolites in tumor ECs for 65 metabolites in 28 metabolism pathways.

(C,D) RNA was extracted from human ECs derived from tumors or normal brains, or treated with or without tumor-conditioned medium (-CM), followed by bulk RNA-seq analysis. Metabolic genes from KEGG database were analyzed.

(C) Genes wtih >50% changed expression by tumor-CM treatment and in tumor-derived ECs were analyzed and plotted in KEGG metabolism modules.

(D) Heatmap of gene expression for top two upregulated modules.

(E,F) Human normal brain and tumor ECs were lyzed.

(E) Cell lysates were immunoblotted.

(F) RNA was extracted and analyzed by RT-PCR. PHGDH expression was normalized with vinculin expression (mean ± SEM, n = 3–4 human samples with 4 technical replicates). Statistical analysis between normal brain and tumor ECs was performed by unpaired two-tailed Student’s t test.

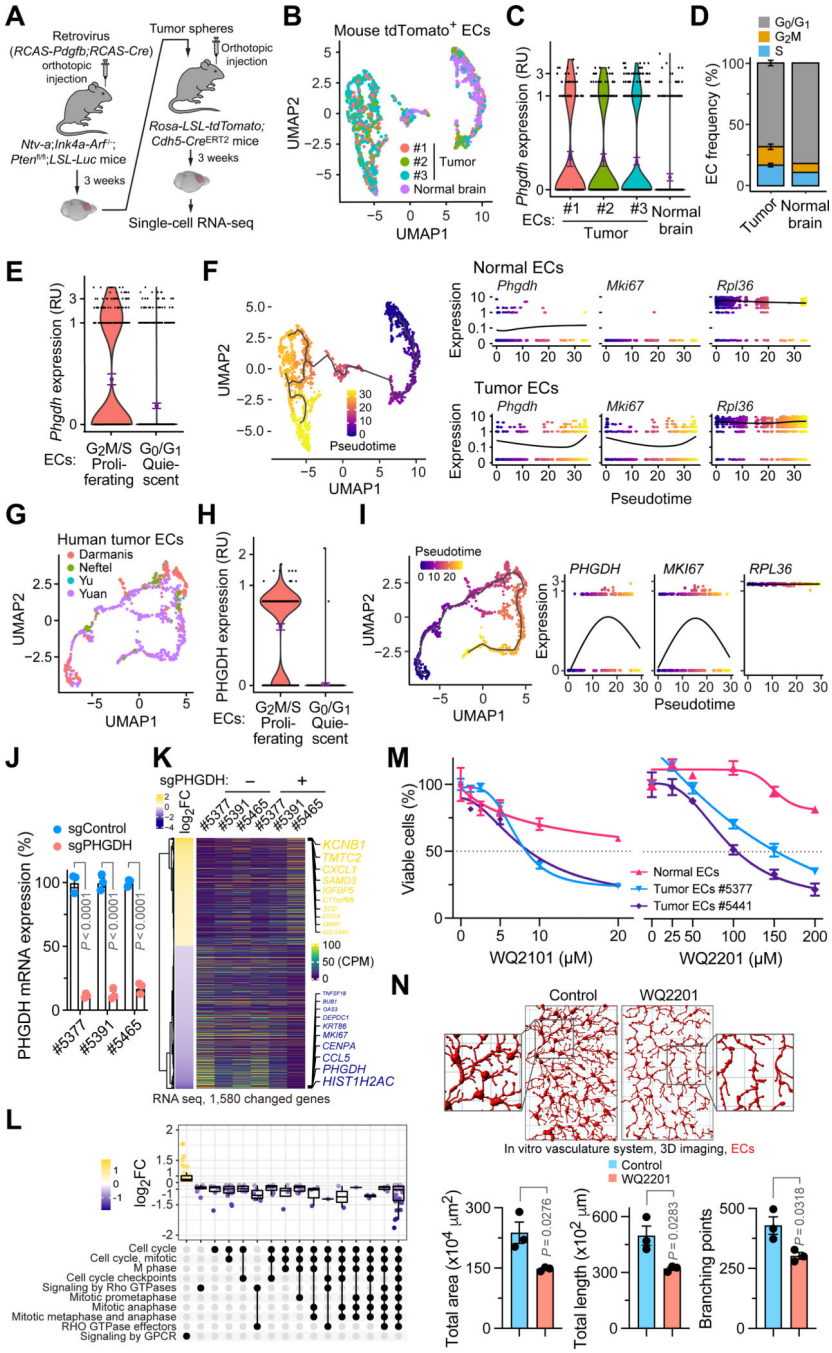

Figure 2. Single-cell and bulk RNAseq reveals a critical and selective role of PHGDH for cell proliferation in tumor ECs.

(A-F) GBM was genetically induced in *Ntv-a;Ink4a-Arf*$^{-/-}$*;Pten*$^{fl/fl}$*;LSL-Luc* mice, followed by tumor implantation into *Rosa-LSL-tdTomato*;*Cdh5-Cre*^{ERT2} mice. Tumor-derived single-cell suspension was analyzed by single-cell RNAseq (n = 4 mice).

(A) Schematic approach.

(B) Uniform manifold approximation and projection (UMAP) analysis of transcriptome gene signature in tdTomato^{+} ECs.

(C) PHGDH expression in ECs derived from normal brain and GBM tumors.

(D) EC distribution in difference cell cycle phases (mean ± SEM).
(E) PHGDH expression in proliferating and quiescent ECs from all samples.
(F) Left, tdTomato+ ECs were re-clustered and subjected to cell trajectory construction. Right, gene expression kinetics of Phgdh, Ki67 (Mki67), and Ribosomal Protein L36 (Rpl36) are expressed as a function of pseudotime in (top) normal brain and (bottom) tumor ECs.
(G-I) Meta-analysis of integrated single-cell RNAseq data of human GBM (n = 60 patients).
(G) UMAP analysis of tumor ECs.
(H) PHGDH expression in proliferating and quiescent ECs.
(I) Tumor ECs were subjected to cell trajectory construction analysis. Gene expression kinetics of Phgdh, Ki67, and Rpl36 are expressed as a function of pseudotime.
(J-L) ECs derived from human GBM tumors were treated with CRISPR sgRNA targeting PHGDH or control sequence.
(J) RNA was analyzed by RT-PCR (n = 3, mean ± SEM). Statistical analysis by two-way ANOVA.
(K,L) RNA was extracted and analyzed by bulk RNAseq.
(K) Heatmap of genes with >50% expression changes.
(L) Pathway analysis of the altered genes, visualizing the complex association between genes and gene sets, with the graph showing the average expression changes of the top regulated genes, and with the dots showing the pathways these genes are mapped to.
(M) Human ECs derived from normal brains or GBM tumors were treated with PHGDH inhibitors, WQ2101 and WQ2201, followed by cell viability analysis (n = 3, mean ± SEM). Results are expressed as % of the values at time 0.
(N) GBM ECs were labeled with CellTrace Far Red and co-cultured in an in vitro flow system, followed by treatment with or without WQ2201 and imaging. Top, Representative images. Grid indicates 100 mm. Bottom, quantified results (n = 3, mean ± SEM). Statistical analysis by unpaired Student’s t test.

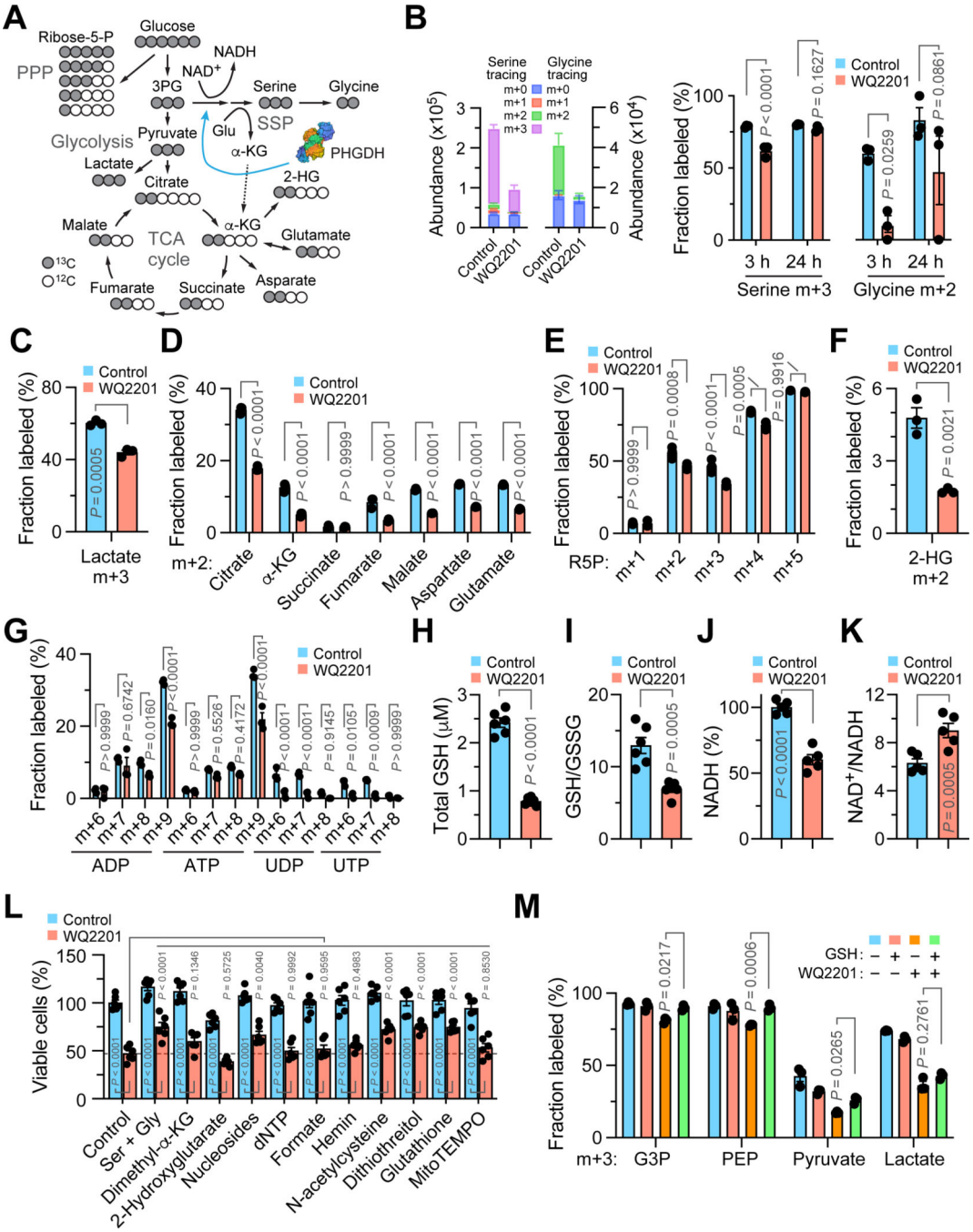

Figure 3. PHGDH modulates redox homeostasis and glycolytic carbon flux to regulate proliferation in tumor ECs.

(A-G) Human tumor ECs derived from patients with GBM were treated with WQ2201 and subjected to [U-13C]-glucose isotopomer tracing.

(A) Schematic carbon flux and role of PHGDH in metabolism pathways. Pentose phosphate pathway, PPP; Serine synthesis pathway, SSP; TCA cycle, tricarboxylic acid cycle.

(B-G) Relative integrated peak intensities for (B) SSP-, (C) glycolysis-, (D) TCA cycle-, (E) PPP-, (F) 2-HG-, and (G) nucleotide synthesis-related metabolites. Statistical analysis by Student's t-test (n = 3 EC samples, mean ± SEM).

(B) Left, abundance of serine and glycine were analyzed 3 h after glucose tracing. Right, quantified fraction of labeled m+3 serine and m+2 glycine.
(C-G) Metabolites were analyzed 24 h after glucose tracing.
(H-K) Human tumor ECs were treated with or without WQ2201 for 24 h, followed by biochemical analysis of (H) total GSH, (I) ratio of GSH/GSSG, (J) NADH, and (K) ratio of NAD+/NADH. Statistic analysis by Student's t-test (n = 5–6 EC samples, mean ± SEM).
(L) Human tumor ECs were treated with WQ2201 in the medium supplemented with different molecules for 96 h, followed by cell viability analysis. Statistical analysis by two-way ANOVA (n = 6 assays, mean ± SEM).
(M) Human tumor ECs were treated with WQ2201 in the medium supplemented with GSH for 24 h, followed by [U-13C]-glucose isotype tracing for 24 h. Shown are relative integrated peak intensities for glycolysis. Statistical analysis by two-way ANOVA (n = 3 EC samples, mean ± SEM).

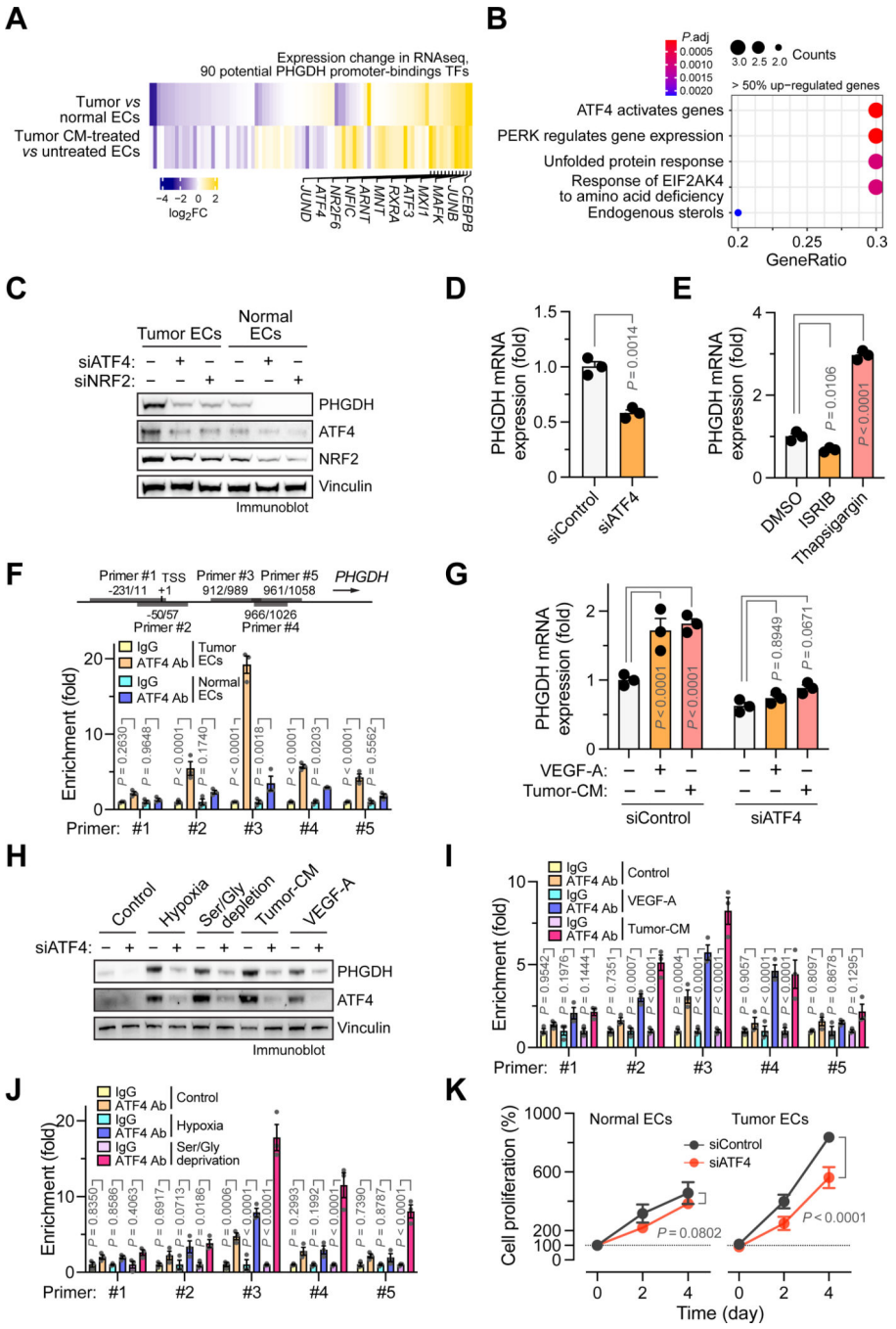

Figure 4. ATF4 induces PHGDH expression in ECs under GBM conditions.

(A,B) RNA was extracted from ECs derived from GBM tumors (n = 5 human patients) or normal brains (n = 3 humans), or treated with or without tumor-conditioned medium (n = 3 humans), followed by RNA-seq analysis.

(A) Gene expression levels of ENCODE-predicated transcriptional factors (TFs) that potentially bind to PHGDH promoter. Top upregulated (> 50% in both groups) TFs are listed.

(B) Pathway analysis of top up-regulated TFs.

(C) Human GBM- and normal brain-derived ECs were treated with siRNA targeting ATF4, NRF2, or control sequence. Cell lysates were immunoblotted.

(D,E) Human GBM-derived ECs were treated with (D) siRNA targeting ATF4 or control sequence, or (E) ISRIB or thapsigargin. RNA was analyzed by RT-PCR. Statistical significance was determined by (D) Student's t test or (E) one-way ANOVA (n = 3 human patients, mean ± SEM).

(F) Nuclei extracts from normal or tumor ECs were immunoprecipitated with an anti-ATF4 antibody or a control antibody, followed by ChIP analysis of ATF4 binding to the PHGDH promoter (n = 3 EC samples, mean ± SEM). Statistical analysis by two-way ANOVA. Ab, antibody.

(G,H) Human normal brain ECs were pre-treated with siRNA targeting ATF4 or control sequence, followed by (G) incubation with VEGF or tumor-conditioned medium (tumor-CM) and (H) exposure to hypoxia or serine- and glycine-free medium. Statistical analysis by one-way ANOVA (n = 3 EC samples, mean ± SEM).

(G) RNA was analyzed by RT-PCR.

(H) Cell lysates were immunoblotted.

(I,J) Human normal brain ECs were treated with (I) VEGF, tumor-CM, (J) hypoxia, or serine/glycine-depleted medium. Nuclei extracts were immunoprecipitated and analyzed by ChIP (n = 3 EC samples, mean ± SEM). Statistical analysis by two-way ANOVA.

(K) Human normal brain ECs or GBM ECs were treated with siRNA targeting ATF4 or control sequence, followed by calcein AM cell proliferation analysis (n = 5 EC samples, mean ± SD). Statistical analysis by Student's t test.

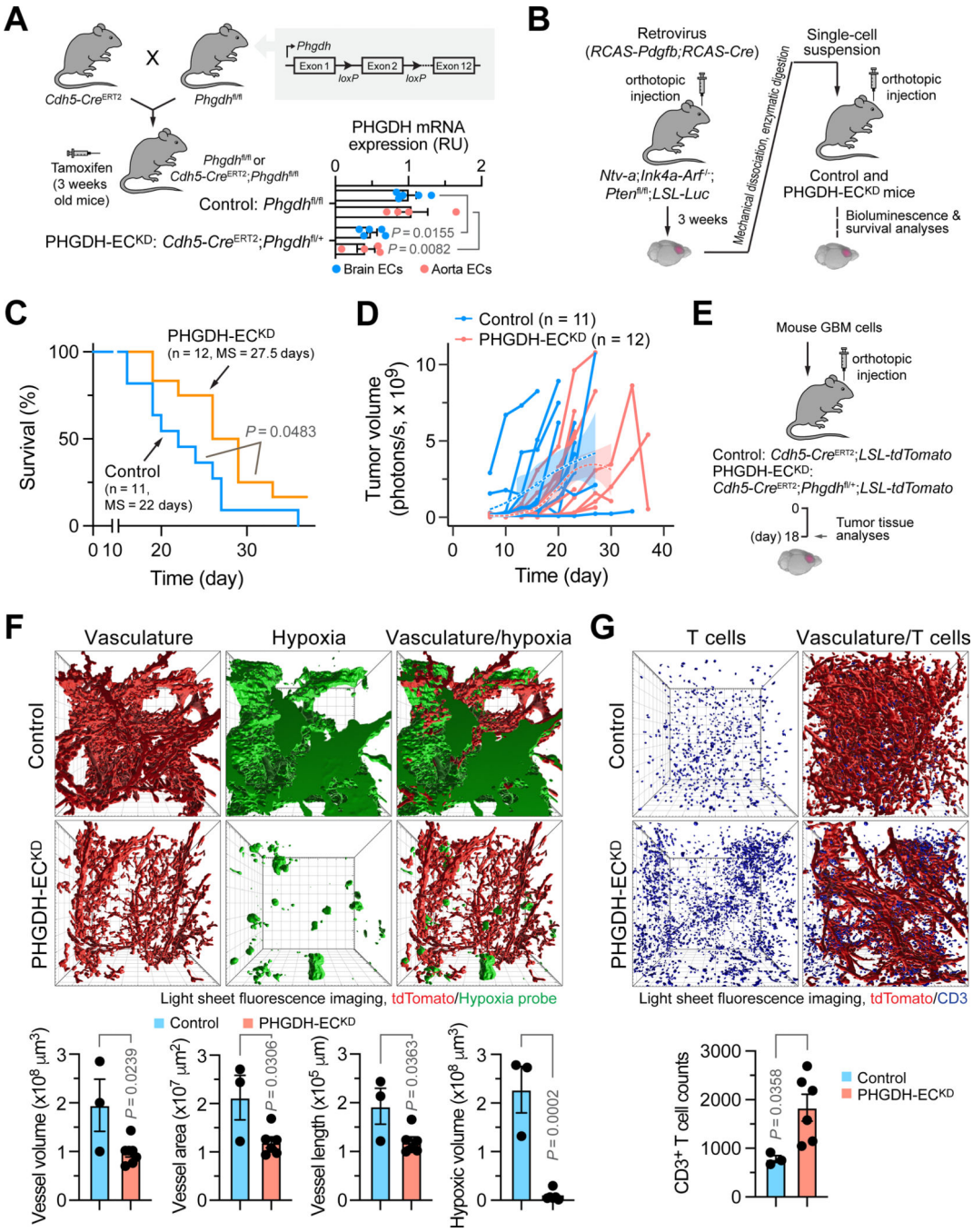

Figure 5. Endothelial-specific knockdown of PHGDH reduces vascular aberrancy and attenuates GBM growth.

(A,B) Phgdhfl/fl mice were generated by insertion of loxP sites into mouse genome, followed by crossing with Cdh5-CreERT2 mice.

(A) Schematic approach for generation of *Phgdh*$^{fl/fl}$ (control) or *Chd5-Cre*^{ERT2};*Phgdh*$^{fl/+}$ (PHGDH-EC^{KD}) mice. 2 weeks old mice were treated with tamoxifen. Inset: ECs were isolated from mouse brains and aortas, and subjected to RT-PCR analysis (n = 4–5 mice). Statistical analysis by two-way ANOVA.

(B-D) Primary GBM was induced in *Ntv-a*;*Ink4a-Arf*$^{-/-}$;*Pten*$^{-/-}$;*LSL-Luc* donor mice by RCAS-mediated somatic gene transfer. Single-cell tumor suspension was transplanted into control and PHGDH-EC^{KD} recipient mice.

(B) Schematic approach.

(C) Animal survival was monitored for 60 days after injection (n = 11–12 mice). MS, median survival. Statistical analysis by LogRank.

(D) Tumor growth was analyzed by whole-body bioluminescence imaging. Dashed lines with shadow area indicate non-linear Loess regression with 95% Cl range (n = 11–12 mice).

(E-G) GBM was genetically induced by RCAS-mediated somatic gene transfer, followed by transplantation into control or PHGDH-EC^{KD} recipient mice. Tumors were excised and analyzed by light sheet fluorescence imaging.

(E) Schematic approach.

(F) Vasculature and hypoxia were imaged in tumors. Top, representative images. Bottom, quantitative results for tumor vascular characters and hypoxia in 1 mm^3 tissues (n = 3 mice for control group, n = 6 mice for PHGDH-EC^{KD} group, mean ± SEM). Statistical analysis by two-tailed Student's t test.

(G) Tumor tissues were stained with anti-CD3 antibody, followed by imaging. Top, representative images. Bottom, quantitative results in 1 mm3 tissues (n = 3 mice for control group, n = 6 mice for PHGDH-EC^{KD} group, mean ± SEM). Statistical analysis by two-tailed Student's t test.

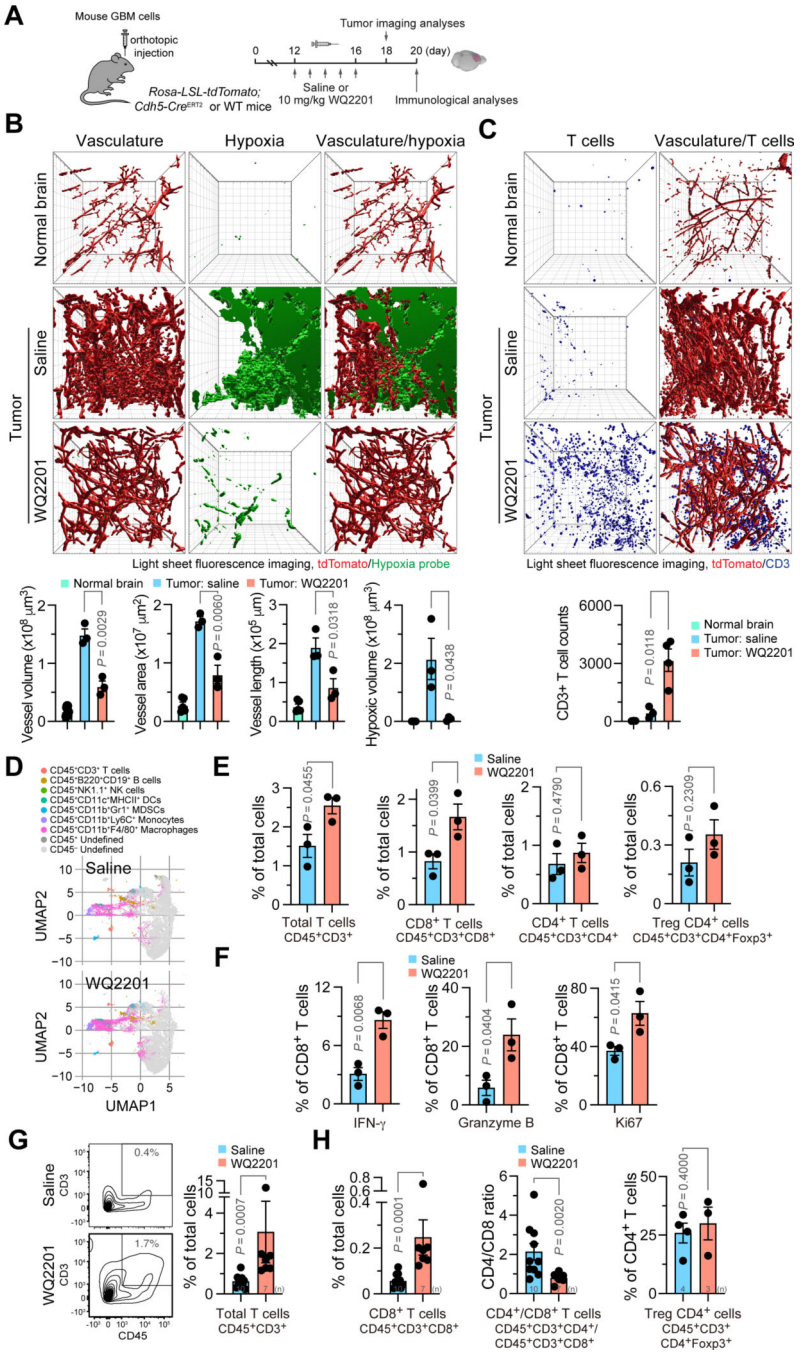

Figure 6. PHGDH inhibition prunes tumor vasculature and improves T cell infiltration and activation in GBM.

(A-H) GBM was genetically by RCAS-mediated somatic gene transfer, followed by transplantation into (B,C) *Rosa-LSL-tdTomato*;*Cdh5-Cre*^{ERT2} and (D-H) WT C57BL/6 recipient mice. Mice were treated with saline or WQ2201, and tumors were excised and analyzed.

(A) Schematic approach.

(B) Vasculature and hypoxia were imaged in tumors. Top, representative images. Bottom, quantitative results for tumor vascular characters and hypoxia in 1 mm^3 tissues (n = 5 mice

for normal brain group, n = 3 mice for other groups, mean ± SEM). Statistical analysis by two-tailed Student's t test.

(C) Tumor tissues were stained with anti-CD3 antibody, followed by imaging. Top, representative images. Bottom, quantitative results in 1 mm^3 tissues (n = 3 mice for normal brain and saline group, n = 4 mice for WQ2201 group, mean ± SEM). Statistical analysis by two-tailed Student's t test.

(D-H) Tumor-derived single-cell suspensions were analyzed using (D-F) CyTOF and (G,H) flow cytometry.

(D) Representative CyTOF results.

(E,F) CyTOF analysis of T cells (n = 3 mice, mean ± SEM). Statistical analysis by two-tailed Student's t test.

(G,H) Flow cytometry analysis of (G) total and (H) subpopulation T cells (mean ± SEM, n = 3–10 mice, specific n value is indicated). Statistical analysis by two-tailed Mann-Whitney t test.

(G) Left, representative sortings. Right, Quantitative results.

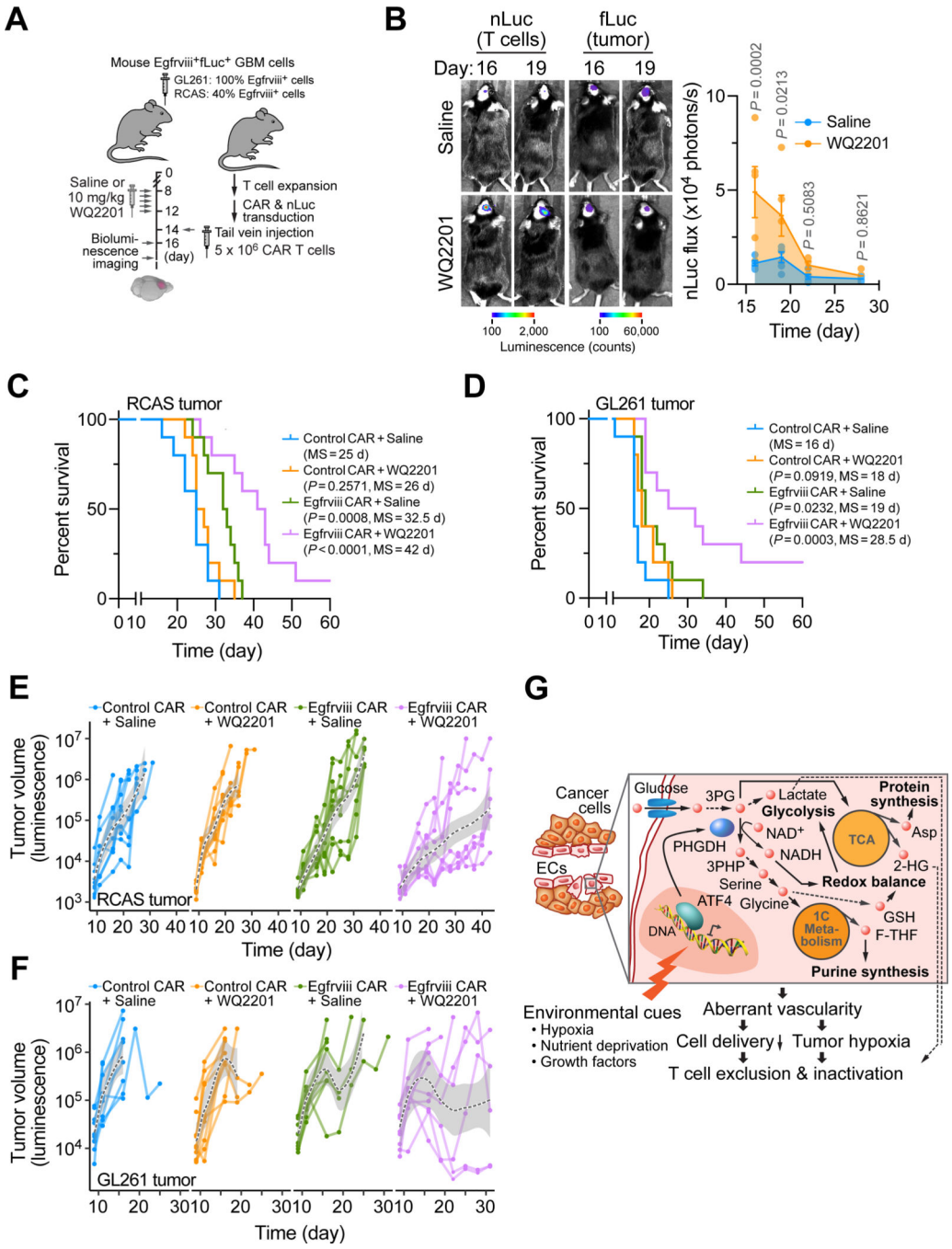

Figure 7. PHGDH inhibition improves EGFRviii CAR T immunotherapy in GBM.

GBM was induced in mice by transplantation of RCAS/Tva-induced murine tumors or GL261 glioma cells. After tumor induction, mice were treated with saline or WQ2201, followed by CAR T cell therapy.

(A) Experimental approach.

(B) T cell trafficking in RCAS tumors was imaged by bioluminescence. Left, representative sortings. Right, quantitative results (n = 5 mice, mean ± SEM). Statistical analysis by two-way ANOVA.

(C,D) Mouse survival was monitored for 60 days in (C) RCAS and (D) GL261 model. Statistical analysis by LogRank (n = 10 mice).
(E,F) Tumor growth was analyzed by bioluminescence imaging in (E) RCAS and (F) GL261 model. Dashed lines with shadow area indicate non-linear Loess regression with 95% Cl range (n = 10 mice).
(G) A schematic model.

Key resources table

REAGENT or RESOURCE	SOURCE	IDENTIFIER
Antibodies		
Anti-PHGDH	Atlas Antibodies	Cat# HPA021241, RRID: AB_1855299
Anti-Vinculin	Atlas Antibodies	Cat# HPA002131, RRID: AB_1080570
Anti-ATF4	Cell Signaling	Cat# 11815, RRID: AB_2616025
Anti-NRF2	Cell Signaling	Cat# 12721, RRID: AB_2715528
Anti-Rabbit IgG (H+L)-HRP Conjugate	BioRad	Cat# 1706515, RRID: AB_11125142
GFP-conjugated Anti-pimonidazole	NPI	Cat# FITC MAb-1, RRID: AB_2801307
Anti-CD3e	Cell Signaling	Cat# 78588, RRID: AB_2889902
APC-conjugated F(ab')2-Goat anti-Rabbit IgG (H+L)	Thermo Scientific	Cat# 31984, RRID: AB_429727
Anti-CD3	BioLegend	Cat# 100233, RRID: AB_2561387
Anti-CD3e	eBioscience	Cat# 14-0031, RRID: AB_467051
Anti-CD28	eBioscience	Cat# 14-0281, RRID: AB_467191
Anti-CD45	eBioscience	Cat# 48-0451-82, RRID: AB_1518806
Anti-CD8a	BioLegend	Cat# 100706, RRID: AB_312745
Anti-CD4	BioLegend	Cat# 100411, RRID: AB_312696
Anti-FOXP3	BioLegend	Cat# 126407, RRID: AB_1089116
Anti-NK1.1	BioLegend	Cat# 108707, RRID: AB_313394
Anti-F4/80	BioLegend	Cat# 123107, RRID: AB_893500
Anti-CD11b	BioLegend	Cat# 101228, RRID: AB_893232
Anti-CD11c	eBioscience	Cat# 17-0114-81, RRID: AB_469345
Anti-CD45R/B220	BioLegend	Cat# 103228, RRID: AB_492874
APC-conjugated goat anti-human F(ab′)2	Jackson Immuno-Research	Cat# 109-136-097, RRID: AB_2337692
Anti-mCD3ε F(ab')2 fragment	BioXCell	Cat# BE0001-1FAB, RRID: AB_2687679
Hamster IgG f(ab')2 fragments	BioXCell	Cat# BE0091-1FAB, RRID: AB_2687680
Anti-mVEGFR-2	BioXCell	Cat# BE0060, RRID: AB_1107766
Rat IgG1 isotype	BioXCell	Cat# BE0088, RRID: AB_1107775
Bacterial and virus strains		
pMSGV1-139 Egfrviii CAR retrovirus	Ma et al, 2021 [50]	N/A
pMSGV1-GFP CAR retrovirus	Ma et al, 2021 [50]	N/A
Biological samples		
GBM tumor ECs isolated from human patients #5377, #5391, #5433, #5441, and #5465.	Department of Neurosurgery, The Hospital of University of Pennsylvania	N/A
Chemicals, peptides, and recombinant proteins		
D-(+)-glucose	Sigma Aldrich	Cat# G8270
L-serine	Sigma Aldrich	Cat# S4311
Glycine	Sigma Aldrich	Cat# G8790
dimethyl-α-KG	Sigma Aldrich	Cat# 349631

REAGENT or RESOURCE	SOURCE	IDENTIFIER
2-hydroxyglutarate	Sigma Aldrich	Cat# 94577
EmbryoMax Nucleosides	Sigma Aldrich	Cat# ES-008-D
dNTPs	Thermo Scientific	Cat# 10297018
Formate	Sigma Aldrich	Cat# 71539
Hemin	Sigma Aldrich	Cat# 51280
N-acetylcysteine	Sigma Aldrich	Cat# A7250
Dithiothreitol	Sigma Aldrich	Cat# 43816
Glutathione	Sigma Aldrich	Cat# G4251
MitoTEMPO	Sigma Aldrich	Cat# SML0737
ISRIB	Sigma Aldrich	Cat# SML0843
Thapsigargin	Sigma Aldrich	Cat# T9033
[U-13C] D-glucose	Cambridge isotope laboratories	Cat# CLM-1396
Pimonidazole HCl	NPI	Cat# HP-200mg
Recombinant Human VEGF 165	Peprotech	Cat# 100-20
PKUMDL-WQ-2201	Biotechne	Cat# 6581
rhIL-2	Peprotech	Cat# 200-02
RetroNectin® Recombinant Human Fibronectin Fragment	Takara	Cat# T100A
Tamoxifen	Sigma	Cat# T5648
Protamin sulfate	MP biomedicals	Cat# 02194729-CF
Furimazine	TargetMol	Cat# T15359
D-luciferin	GoldBio	Cat# LUCNA-5G
TRIzol	Thermo Fisher	Cat# 15596026
Intercalator-Ir	Fluidigm	Cat# 201192A
Cisplatin	Fluidigm	Cat# 201064
Lipofectamine 3000	Life Technologies	Cat# L3000001
RNAiMAX Lipofectamine	Invitrogen	Cat# 13778075
Puromycin Dihydrochloride	Gibco	Cat# A1113803
CellTrace Far Red dye	Invitrogen	Cat# C34572
Matrigel	Corning	Cat# 356231
NP-40 lysis buffer	Thermo Scientific	Cat# J60766.AP
Protease inhibitor	Roche	Cat# 11697498001
ECL Western Blotting Substrate	GE Healthcare	Cat# RPN2232
Collagenase-II	Invitrogen	Cat# 17101-015
DNase	Sigma Aldrich	Cat# D4527
dispase II	Gibco	Cat# 17105-041
D-(+)-glucose	Sigma Aldrich	Cat# G8270
Critical commercial assays		
RNeasy Plus Mini Kit	Qiagen	Cat# 74134
Magna ChIP kit	Millipore	Cat# MAGNA0001

REAGENT or RESOURCE	SOURCE	IDENTIFIER
Fast SYBR Green Master Mix	Applied Biosystems	Cat# 4385612
SuperScript III First-Strand Synthesis SuperMix	Invitrogen	Cat# 18080400
FITC-BrdU flow kit	BD Pharmingen	Cat# 559619
EasySep Mouse T Cell Isolation Kit	Stemcell technologies	Cat# 19851
Calcein AM cell viability assay kit	Trevigen	Cat# 4892-010-K
GSH/GSSG-Glo™ Assay kit	Promega	Cat# V6611
NAD/NADH-Glo™ Assay kit	Promega	Cat# G9071
CellTiter-Glo® Assay kit	Promega	Cat# G7570
Deposited data		
Bulk RNA sequencing analysis of human GBM and normal brain ECs	This paper	GSE199375
Bulk RNA sequencing analysis of human GBM ECs treated with control CRISPR/sgRNA or CRISPR/sgRNA targeting PHGDH	This paper	GSE199376
Single-cell RNA sequencing analysis of mouse normal brain and GBM tumors	This paper	GSE199379
Human glioblastoma scRNA-seq data for meta-analysis	Darmanis et al., 2017 [85]	GSE84465
Human glioblastoma scRNA-seq data for meta-analysis	Yuan et al., 2018 [86]	GSE103224
Human glioblastoma scRNA-seq data for meta-analysis	Neftel et al., 2019 [87]	GSE131928
Human glioblastoma scRNA-seq data for meta-analysis	Yu et al., 2020 [88]	GSE117891
Experimental models: Primary cells and cell lines		
Human brain microvascular ECs	Department of Neurosurgery, The Hospital of University of Pennsylvania	N/A
Human brain microvascular ECs	ScienCell	Cat# 1000
Human brain microvascular ECs	Cell Biologics	Cat# H6023
Normal human astrocytes	Lonza	Cat# CC-2565
Platinum-ECO cells	Cell Biolabs	Cat# RV-101, RRID: CVCL_B488
GL261 mouse glioma cells	Perkin Elmer	Cat# 134246, RRID: CVCL_X986
U-251MG human glioma cells	Sigma Aldrich	Cat# 09063001, RRID: CVCL_0021
DF-1	ATCC	Cat# CRL-12203, RRID: CVCL_0570
Experimental models: Organisms/strains		
Phgdh$^{fl/fl}$ mice	This paper, by University of Pennsylvania Transgenic and Chimeric Mouse Facility	N/A
Rosa-LSL-tdTomato mice	Jackson Laboratory	RRID:IMSR_JAX:007914
Cdh5-Cre^{ERT2} mice	Provided by Ralf Adams from Max Planck Institute	N/A
Ntv-a;*Ink4a-Arf*$^{-/-}$;*Pten*$^{fl/fl}$;*LSL-Luc* mice	Provided by Eric Holland from Fred Hutchinson Cancer Research Center	N/A
C57BL/6J mice	Jackson Lab	RRID: IMSR_JAX: 000664
Oligonucleotides		
siRNA-PHGDH	Dharmacon	Cat# L-009518-00-0005
siRNA-ATF4	Dharmacon	Cat# L-005125-00-0005

REAGENT or RESOURCE	SOURCE	IDENTIFIER
siRNA-NRF2	Dharmacon	Cat# L-003755-00-0005
Control siRNA	ThermoFisher	Cat# AM4611
Recombinant DNA		
pMMLV-tdTomato-T2A-nLuc plasmid	This paper, by Vectorbuilder	Custom order
Software and algorithms		
Prism 9	GraphPad	N/A
Flowjo 10	FlowJo	N/A
R version 4.0.5	R Development Core Team	https://www.r-project.org/
CellRanger v6.1.2	10x Genomics	https://www.10xgenomics.com
Imaris 9.8	Oxford Instruments	https://imaris.oxinst.com/
Other		
Dialyzed FBS	Gibco	Cat# A3382001
Glucose-, serine-, and glycine-free Endothelial Cell Growth Medium 2	PromoCell	Custom order
Endothelial Cell Medium	Sciencell	Cat# 1001
idenTx 3 Chip	AIM Biotech	Cat# DAX-1